New eastern China agricultural burning fire emission inventory and trends analysis from combined geostationary (Himawari-8) and polar-orbiting (VIIRS-IM) fire radiative power products

Tianran Zhang[1, 2], Mark C. de Jong[1, 2], Martin J. Wooster[1, 2], Weidong Xu[1, 2], Lili Wang[3]

[1] King's College London, Leverhulme Centre for Wildfires, Environment and Society, Dept of Geography, Aldwych, London WC2B 4BG.

[2] NERC National Centre for Earth Observation (NCEO)

[3] LAPC, Institute of Atmospheric Physics, Chinese Academy of Sciences, Beijing 100029, PR China

Correspondence to: Tianran Zhang (tianran.zhang@kcl.ac.uk)

Abstract

Open burning of agricultural crop residues is widespread across eastern China, and during certain post-harvest periods this activity is believed to significantly influence air quality. However, the exact contribution of crop residue burning to major air quality exceedances and air quality episodes has proven difficult to quantify. Whilst highly successful in many regions, in areas dominated by agricultural burning MODIS-based fire emissions inventories such as GFAS and GFED are suspected of significantly underestimating the magnitude of biomass burning emissions due to the typically very small, but highly numerous, fires involved that are quite easily missed by coarser spatial resolution remote sensing observations. To address this issue, we here use twice daily fire radiative power (FRP) observations from the 'small fire optimised' VIIRS-IM FRP product, and combine it with fire diurnal cycle information taken from the geostationary Himawari-8 satellite. Using this we generate a unique high spatio-temporal resolution agricultural burning inventory for eastern China for the years 2012-2015, designed to fully take into account small fires well below the MODIS burned area or active fire detection limit, focusing on dry matter burned (DMB) and emissions of CO_2, CO, $PM_{2.5}$ and black carbon. We calculate DMB totals 100 to 400% higher than reported by GFAS and GFED4.1s, and quantify interesting spatial and temporal patterns previously un-noted. Wheat residue burning, primarily occurring in May-June, is responsible for more than half of the annual crop residue burning emissions of all species, whilst a secondary peak in autumn (Sept-Oct) is associated with rice and corn residue burning. We further identify a new winter (Nov-Dec) burning season, hypothesised to be caused by delays in burning driven by the stronger implementation of residue burning bans during the autumn post-harvest season. Whilst our emissions estimates are far higher than those of other satellite-based emissions inventories for the region, they are lower than estimates made using traditional 'crop yield-based approaches' (CYBA) by a factor of between 2 and 5x. We believe that this is at least in part caused by outdated and overly high burning ratios being used in the CYBA approach, leading to the

33 overestimation of DMB. Therefore we conclude that that satellite remote sensing approaches which adequately detect

34 the presence of agricultural fires are a far better approach to agricultural fire emission estimation.

35

36 **Keywords**: Agriculture, Biomass Burning, Active Fire, VIIRS, Air Quality, Fire Emission

37

38 **1. INTRODUCTION**

39 Eastern China (111 - 123 °E, 27 – 40 °N) is home to around one third of the Chinese population and includes the area

40 of the North China Plain and the Yangtze Plain - two of the largest agricultural zones in China (Fig. 1). Cropland

41 covers over 1.7 million km^2 of eastern China, and the region is responsible for an estimated 25% of China's crop

42 production, including around 51% of the national rice yield (NBSC, 2012). Large amounts of crop residue (~ 60

43 Tg/year including stems, stalks, straw etc) results from this agricultural production (Chen et al., 2017; Huang et al.,

44 2012; Zhang et al., 2015), and the burning of this waste in open fields is widespread across much of eastern China

45 (Fig. 2).

46 This biomass burning has both local and regional scale air quality impacts, with emissions of particulate matter (PM)

47 of particular concern (Bond et al., 2013). The East Asian monsoon system that influences much of mainland China

48 results in prevailing north-westerly to south-easterly atmospheric transport during winter, which is reversed in the

49 summer months. Under these influences, the smoke from agricultural residue fires in Eastern China often affects

50 "mega-cities" like Beijing and Shanghai (Chan & Yao, 2008; Cheng et al., 2013; Du et al., 2011; Li et al., 2010).

51 Modelling studies show that these agricultural emissions can drive intense regional air pollution episodes; Huang et

52 al. (2012) suggest that PM_{10} concentrations in some cities could reach 600 µg m^{-3} during such episodes, a level 6×

53 higher than the WHO 24h-mean PM_{10} air quality guideline for human health (WHO, 2005).

54 Agricultural burning in eastern China accounts for a significant part of China's total biomass burning emissions

55 (Streets et al., 2003; Chen et al., 2017), however the specific contribution of crop residue burning to air quality

56 exceedances in China remains uncertain, partly because there is considerable doubt as to the amount of dry matter

57 burned (DMB) in crop residue fires. For example, this leads to a ~450 % range in total crop residue burning black

58 carbon emissions in Asia between different emissions inventories (Streets et al., 2003), while emissions estimates of

59 gaseous species are similarly varied.

60 A major source of this uncertainty stems from the hitherto relatively poor ability of earth observation (EO) satellite

61 instruments to adequately detect biomass burning activity in many agricultural areas due to the small size of the fires

62 usually found in these areas. Many agricultural fields in eastern China are typically only around 700 m^2 in area (NBSC,

63 2012), and fires ignited to burn across the stubble left in the place after harvest are therefore hard to detect with

64 moderate spatial resolution burned area (BA) mapping from sensors such as MODIS (Moderate Resolution Imaging

65 Spectroradiometer), and are made even more elusive by the common farming practice of pilling up residues into an

66 even smaller area before igniting them (Zhang et al., 2017; 2018). As most BA mapping methods require ~ > 20 % of

67   a pixel to be burned in order for it to be classified as 'fire affected' (Giglio et al., 2006; 2009), BA-based emissions

68   inventories such as GFED (Global Fire Emissions Database) tend to significantly underestimate fire activity in areas

69   such as eastern China (Zhang et al., 2018).

70   Infrared based Active fire (AF) based detection techniques can discriminate fires covering only 0.01-0.1 % of a pixel

71   area (Wooster et al., 2005; Schroeder et al., 2014), and as such should in theory be able to capture far more fire activity

72   in agricultural areas than BA based methods. Nevertheless, due to the extremely small size of agricultural fires in

73   eastern China, a large proportion of fire activity remains undetected by AF detection algorithms applied to 'moderate'

74   spatial resolution imagery (from sensors such as MODIS). This limitation is a key source of uncertainty within the

75   FRP approach, and indeed in fact can lead to biased (underestimated) FRP totals caused by the non-detection of the

76   lower FRP component of a regions fire regime (e.g. Roberts et al., 2015). Higher spatial resolution polar-orbiting

77   sensors such as VIIRS (Visible Infrared Imaging Radiometer Suite) can provide the ability to identify an increased

78   number of AFs having lower FRP values, particularly when used with algorithms optimised for small fire detection

79   (Zhang et al., 2017) (Fig. 2), but they still only capture fires burning in clear skies at the time of the satellite overpass

80   (Giglio et al., 2003; 2006). This limitation is also a considerable source of uncertainty, and a hinderance given the

81   sometimes short duration of active burning (especially of agricultural fires) and the typical polar orbiting imaging

82   frequency of only a few times per day. To cope with this issue, FRP-based emissions inventories such as GFAS based

83   upon AF methods are generally required to make assumptions or exploit additional data on the timing and relative

84   diurnal variability of fire activity occurring between polar orbiting overpasses in order to estimate, for example, total

85   daily Fire Radiative Energy (FRE) (Kaiser et al., 2012; Xu et al., 2017; Zhang et al., 2017). Here we provide this

86   additional information by exploiting new fire diurnal cycle information taken from the geostationary satellite

87   Himawari-8, combining it with twice daily FRP information provided by the 'small fire optimised' VIIRS-IM product

88   of Zhang et al. (2017) to produce a unique high spatio-temporal resolution agricultural fire dataset (referred to hereafter

89   as the VIIRS-IM/Him dataset) for eastern China based on FRE totals. This new inventory is designed to reduce bias

90   and uncertainty caused by use of one FRP data type alone, and to account for small fires burning even for short periods

91   and often well below the MODIS AF and BA detection limit. The fuel for these fires is waste straw and other

92   agricultural residues, and we use a crop rotation map to classify the type of agricultural residue being burned at each

93   observed location and time. It is then used to select the most appropriate smoke emissions factor for calculating the

94   final fire emissions totals from FRE derived estimates of dry matter burned (DMB).

95

2. DATASETS

2.1 Polar Orbiting VIIRS-IM FRP Product

The Visible Infrared Imaging Radiometer Suite (VIIRS) instrument is currently flown aboard the polar orbiting Suomi NPP (since 2011) and NOAA-20 (since 2017) satellites and expands upon the capabilities of the AVHRR and MODIS instruments for environmental monitoring (Zhou et al., 2019). VIIRS has 22 channels spanning the visible to the longwave infrared, a 3000 km swath width, and nadir pixel resolution ranging between 375 m and 750 m (Goldberg et al., 2013). Furthermore, a 'pixel aggregation' scheme is applied to VIIRS which limits pixel area increase with scan angle to a maximum of 4× compared to MODIS' 10× (Wolfe et al., 2013).

With a necessary emphasis on the detection of small fires typical of agricultural regions, our work focuses on generating a gridded daily biomass burning fuel consumption product that estimates DMB and emissions from the VIIRS-IM AF Detection and FRP product developed and optimised for eastern China by Zhang et al. (2017), using data from the instrument aboard the Suomi NPP satellite with a mean local daytime overpass time of 13:30 in the ascending node, and a mean local nighttime overpass time of 01:30 in the descending node (Wolfe et al., 2013). Fig. 2 shows an example of the VIIRS-IM FRP product, generated from the two observations per day provided by Suomi NPP VIIRS. This FRP product blends the advantages of the 'small fire' sensitivity of the VIIRS 375 m I-Band, with the ability to retrieve fire radiative power (FRP) over larger fires using the 750 m M-Band observations. Due to the very small size of agricultural fires in China, and because the VIIRS I-Band pixel area is 10× smaller than the pixel area of MODIS, far more fires can be detected in eastern china using the VIIRS-IM AF product of Zhang et al. (2017) than can be identified in near simultaneous MODIS data, and on average across eastern China retrieves FRP totals around 4× higher (Zhang *et al.*, 2017).

2.2 Geostationary Himawari FRP Product

To convert the twice-daily VIIRS-IM FRP product to daily-integrated FRE, information on the fire diurnal cycle is required (Ellicott et al., 2009; Freeborn et al., 2008; Roberts et al., 2009). We obtained this from 10-min temporal resolution observations from the geostationary Himawari-8 satellite, whose data have recently been used to derive AF detections and FRP metrics across Asia by Xu et al. (2017). Himawari cannot be used in isolation to directly estimate daily FRE for each of the 4-years of the study, because (i) Himawari data are only available from early 2015 onwards, and (ii) Himawari's relatively coarse pixel size (2 km at the sub-satellite point) means that it omits even more of the agricultural fires than does MODIS (as illustrated by Xu et al., 2017 and in Fig.3). However, where agricultural fires are concentrated in sufficient density, observations by Himawari do enable their detection and these data can be used to map the changing FRP of these fires over the day for derivation of the fire diurnal cycle.

2.3 Crop Rotation Map

129   The predominant agricultural residues burned across eastern China are wheat, corn and rice straw (Huang et al., 2012).

130   To classify the likely residue type of each detected fire, a crop rotation map (Fig. S1) was generated from the

131   MIRCA2000 0.08º global monthly crop area dataset (Portmann *et al.,* 2010), which has a spatial resolution equivalent

132   to 9.2 km × 9.2 km at the equator. These data were used to assign fire activity to a particular crop residue type, which

133   determined the appropriate agricultural biomass burning emission factors to apply (see Section 3.3).

134

135   2.4 Land Cover Data

136   We use the GlobeLand30 land cover product (Chen et al, 2015) to classify land cover/use for our study area in Eastern

137   China. GlobeLand30 provides 30m spatial resolution land cover data for a baseline year of 2010 derived primarily

138   from Landsat (TM5 & ETM +) and China Environmental Disaster Alleviation Satellite (HJ-1) imagers. Fig. 1 shows

139   the spatial distribution of the agricultural land ratio (regridded to 0.01 degree spatial resolution) calculated use this

140   dataset in eastern China.

141

142   2.5 GFED & GFAS Emissions Inventory Data

143   The results from the combined VIIRS-IM and Himawari FRP based emissions (VIIRS-IM/Him) dataset were

144   compared to two state-of-the-art global fire emission databases, the Global Fire Emissions Database (GFED) and the

145   Global Fire Assimilation System (GFAS). GFED was built to combine remotely sensed data on BA with fuel loads

146   from the CASA biogeochemical model of vegetation growth, producing monthly, spatially explicit pyrogenic fuel

147   consumption, carbon, GHG and air pollution emission estimates at 0.25º grid cell resolution globally (Van der Werf

148   et al., 2010; Giglio et al., 2013). The most recent version (GFED4.1s) includes a "small fire boost" based on AF

149   detections, in an attempt to counteract the inability of the MODIS BA product to detect many agricultural fires

150   (Randerson et al., 2012; Van der Werf et al., 2017). Due to this 'boost' GFED4.1s shows higher values of dry matter

151   burned (DMB) in most eastern China grid cells compared to the 'unboosted' GFED4, and a more extensive fire

152   distribution. However, Zhang et al. (2018) show that the boosting procedure can introduce significant anomalies into

153   the GFED dataset at certain times of year, generated when MODIS' AF detection procedure incorrectly identifies

154   urban features in eastern China as fires.

155   In contrast to GFED, the GFAS fire emissions database is based on AF detections and is integrated into Copernicus

156   Atmosphere Monitoring Service (CAMS) system for near-real-time atmospheric composition monitoring and

157   forecasting. Developed by Kaiser et al. (2012) and based on the FRP method, MODIS supplies the FRP data for the

158   current GFAS v1.2 up to 4 times per day at most latitudes. From these observations, DMB is calculated via a regression

159   against GFED DMB values (Kaiser et al., 2012) and daily emissions of 40 emitted species are then calculated at 0.1º

160   spatial resolution.

161

162   2.6 Crop Yield Based Approach Emissions Inventory Data

163   The traditional method for estimation of agricultural fire emissions is the so-called crop yield based approach (CYBA),

164   and we compare data from such approaches to our new VIIRS-IM/Him methodology. CYBAs typically calculate the

165   amount of crop residue burned in a region using a combination of crop production statistics and related additional

166   parameters using following equation:

167    $DMB = \sum_{i=1}^{n} P_i R_i B_i C$ (1)

168   Where i stands for each of n different crops; DMB is total dry matter burned (kg) in the region; P_i is the regional

169   production of crop i (kg), and is usually derived from annual agricultural statics reports; R_i is the dry matter production-

170   to-residue ratio (unitless), which depends on the crop type i; B_i is the proportion of residue burned in the field for crop

171   type i in the region under study (i.e. the 'burning ratio'; 0-1, unitless); and C is crop combustion completeness (0-1,

172   unitless, Huang *et al.,* 2012). DMB is then multiplied by appropriate particulate/gaseous emission factors in order to

173   estimate the total emissions from agricultural burning.

174   Certain of the parameters of Eqn. 1 are not so easily determined. For example, the burning ratio (B_i) is often based on

175   questionnaires or investigations on the use of crop residues conducted with farmers (Gao *et al.,* 2002; Wang and Zhang,

176   2008). Because of strong variations in socio-economic development across the huge expanse of mainland China, large

177   differences in the estimates of B_i exist (Jiang *et al.,* 2012; Liu *et al.,* 2008; Yamaji *et al.,* 2010). B_i may also change

178   considerably from year to year since it is strongly impacted by the level of local economic development, the

179   availability of alternative uses for crop residues in the region, and the regional governance of fire prohibition (Chen

180   *et al.,* 2017). Moreover, considering the official prohibition of open air burning, the reliability of data based on surveys

181   that ask farmer how much residue they burn is questionable. Despite this, most studies that include estimation of

182   agricultural fire emissions in Eastern China have relied on the CYBA (e.g. Cao *et al.,* 2006; He *et al.,* 2011; Huang *et*

183   *al.,* 2012; Li *et al.,* 2009; Qin and Xie, 2011; Yan *et al.,* 2006; Zhao *et al.,* 2015).

184

185   **3. METHODOLOGY**

186   3.1 Data Gridding and Cloud Cover Adjustment

187   The VIIRS-IM FRP product data (in MW), originally derived at the pixel scale, were aggregated to 0.1° resolution for

188   this analysis. Unlike the daily average MODIS FRP calculation of GFAS, which weights individually contributing

189   MODIS FRP observations by their view zenith angle to downgrade the importance of far off-nadir measurements

190   (Kaiser *et al.,* 2012), no such weighting was applied to the VIIRS-IM FRP data since they have already shown very

191   limited view zenith angle dependence as a result of the VIIRS' pixel-averaging procedure (Zhang et al., 2017). For

192   each VIIRS overpass, the total observed FRP present in each 0.1° grid cell j (i.e. FRP$_j$) was calculated from the

193   cumulative FRP of all native resolution AF pixels i within the grid cell:

194    $FRP_j = \sum_{i \in j} FRP_i$ (2)

195 Total observed agricultural area (A, excluding cloud covered area) within each 0.1° grid cell was calculated similarly

196 using the GlobeLand30 30m landcover map:

197 $A_j = \sum_{i \in j} A_i$ (3)

198 The VIIRS-IM product is only affected to a limited degree by smoke because of the relative transparency of smoke

199 plumes at Mid-Wave Infrared (MWIR) wavelengths due to the dominant particle size being smaller than the

200 wavelengths of the VIIRS MWIR channel (Zhang et al., 2017). However, the product cannot provide information in

201 cloud covered areas, and so an adjustment is required to take into account actively burning fires hidden from view by

202 clouds. Following Streets *et al.* (2003) we assume that for partially cloud covered grid cells, the AF and FRP

203 distribution under cloud is the same as under the clear sky areas, as is also assumed in GFAS (Kaiser *et al.*, 2012).

204 Subsequently, the gridded and cloud-adjusted FRP areal density (ρ_j, MW.km^{-2}) is calculated using:

205 $\rho_j = \frac{FRP_j}{A_j}$ (4)

206 Cloud cover (CC) fractions in some grid cells occasionally reach 0.5 (50%), but most are zero. After the cloud cover

207 adjustment, the mean FRP areal density across the study area increased by 11.5%, so the overall effect of the CC

208 adjustment is relatively minor.

209 3.2 Diurnal Cycle and Daily FRE Generation

210 Hourly averages of the 10-minute FRP data from the Himawari-8 FRP product of Xu *et al.* (2017) were gridded to the

211 same 0.1° grid cell resolution as the VIIRS-IM dataset. For each grid cell and calendar day, hourly FRP data were

212 normalised in order to minimise the impact of day-to-day variations in fire activity:

213 $\widetilde{FRP_{j,d}^h} = \frac{FRP_{j,d}^h - \min(FRP_{j,d})}{\max(FRP_{j,d}) - \min(FRP_{j,d})}$ (5)

214 Where $\widetilde{FRP_{j,d}^h}$ is the normalised Himawari-8 FRP for hour h on day d for grid cell j; $FRP_{j,d}^h$ is the averaged Himawari-

215 8 FRP (MW) for hour h on day d for grid cell j; $\max(FRP_{j,d})$ and $\min(FRP_{j,d})$ are respectively the maximum and

216 minimum hourly Himawari-8 FRP (MW) observed on day d for grid cell j. Note that h is in local time (UTC/GMT +

217 8 hours) and the diurnal cycle runs from 0 to 23 hours.

218 $\widetilde{FRP_{j,d}^h}$ data for 2015 were used to produce two normalised 'seasonal' diurnal fire cycles for the eastern China study

219 area: a 'summer' diurnal cycle, constructed from May-June data, and an 'autumn' diurnal cycle, constructed from

220 Sept-Oct data. Both normalised seasonal diurnal cycles were calculated using a weighted mean so that days and grid

221 cells with high fire activity had the greatest influence on the cycle:

222 $$FRP^h = \frac{\sum_d \sum_j \left(\widetilde{FRP_{j,d}^h} \times FRP_{j,d}^h \right)}{\sum_d \sum_j \left(FRP_{j,d}^h \right)}$$ (7)

223

224 Where FRP^h is the normalised FRP for hour h for the entire study area and fire season (summer or autumn). Fig. 4

225 shows the resulting weighted mean fire diurnal cycle for the summer season for Eastern China. This diurnal cycle is

226 bi-modal: a primary peak occurs around 13:00 local time that extends from around 08:00 to 18:00 (daytime) and a

227 second much smaller peak occurs around 21:00 local time (with a magnitude of only ~ 20% of the normalised FRP

228 value of the first peak).

229 We blended information from the Himawari FRP diurnal cycle with the instantaneous twice-daily VIIRS-IM FRP

230 areal density (ρ_j, MW.km^{-2}) data, using an approach based on Andela et al. (2015) to create the VIIRS-IM/Him dataset.

231 Here we represent the diurnal fire cycle as a gaussian function parameterised using the Himawari FRP diurnal cycle,

232 superimposed on a fixed baseline. For a given grid cell j, at instantaneous time t, VIIRS-IM/Him FRP areal density is

233 calculated by:

234

235
$$\rho_{VIIRS-Him_{j,t}} = \rho_{VIIRS_{night,j}} + \mu\left(\rho_{VIIRS_{day,j}} - \rho_{VIIRS_{night,j}}\right) e^{-\frac{\left(t - t_{Himpeak}\right)^2}{2\sigma^2}} \tag{8}$$

236

237 Where $\rho_{VIIRS-Him_{j,t}}$ is the instantaneous VIIRS-IM/Him FRP areal density (MW.km^{-2}) for grid cell j at time t;

238 $\rho_{VIIRS_{night,j}}$ is the night-time (~01:00 LST) VIIRS-IM FRP areal density value (MW.km^{-2}) for grid cell j; $\rho_{VIIRS_{day,j}}$

239 is the day time (~13:00 LST) VIIRS-IM FRP areal density value (MW.km^{-2}) for grid cell j; μ is an adjustment factor

240 used to account for the difference between the VIIRS daytime overpass time and the peak time of the weighted mean

241 fire diurnal cycle (Eqn. 9); $t_{Himpeak}$ is the time of day at which the seasonal Himawari FRP diurnal cycle peaks; σ is the

242 standard deviation of the main peak of the Himawari FRP diurnal cycle, calculated by fitting a gaussian function

243 (using non-linear least squares) to the seasonal Himawari FRP diurnal cycles. The summer diurnal cycle σ value

244 (2.39±0.053) was applied during the April-August period, and the autumn diurnal cycle σ value (1.63±0.041) was

245 applied during the September-March period.

246 The adjustment factor μ is used to account for the fact that the VIIRS daytime overpass time is unlikely to coincide

247 with the peak of the fire diurnal cycle:

248

249
$$\mu = e^{\frac{\left(t_{VIIRS_{day,j}} - t_{Himpeak}\right)^2}{2\sigma^2}} \tag{9}$$

250

251 Where $t_{VIIRS_{day,j}}$ is the local time of the VIIRS-IM FRP observation for grid cell j.

252 Daily FRE was then estimated for each grid cell j and calendar day by integrating the instantaneous VIIRS-IM/Him

253 FRP data using Eqn. 8.

254

3.3 Conversion to Dry Matter Burned (DMB) and Smoke Emissions

To convert the estimated FRE areal density to fuel consumption/DMB, we multiplied FRE by the 0.368 (±0.015) kg.MJ^{-1} factor derived by Wooster *et al*. (2005) from a series of outdoor experimental straw fires, that were very similar to the Chinese agricultural residue fires used herein (Zhang et al., 2015). To convert the resultant DMB into smoke emissions, we used the emission factors of wheat and rice derived from *in situ* measurements in agricultural areas by Zhang et al. (2015) (Table 1). Corn residue was not a fuel type measured during those experiments, and so for this fuel type (which was only 16-22% of the total agricultural fuel consumption) we used the emissions factors for agricultural corn fires from Andreae and Merlet (2001), as is used in GFAS (Kaiser *et al.,* 2012) (Table 1). Together with the crop rotation map (see Section 2.3 and Fig. S1) the EFs from Table 1 enabled us to select the appropriate emissions factor for use at a particular location and time of year.

Furthermore, a winter burning season was discovered during November and December (see details in Section 5.1) when no cultivation crop is shown in the MIRCA2000 data in the study region. Analysis in this study shows that winter fires are likely to result from the combustion of stored residues from the autumn harvest season, therefore all fire activity in winter was assigned to crop types (and therefore emission factors) using the crop rotation map from the previous closest month (October) (Fig. S1). This methodological change is accounted for in the data presented in Fig. 5.

4. BIOMASS BURNING AND EMISSIONS RESULTS

4.1 Temporal and Spatial Distribution of FRE In Eastern China

Fig. 5 shows the time series of daily mean FRE areal density in eastern China from February 2012 to December 2015, reported at 0.1° grid cell resolution, and broken down into three main crop residue types. A strong seasonal variation is seen, with peak activity in summer (May-June) associated with wheat residue burning and a smaller secondary peak in activity occurring in autumn (Sept-Oct) associated with corn and rice residue burning. In fact, the secondary peak is a combination of several fluctuations lasting from October until December, further discussed in Section 5.1. Over the whole 4-year period, wheat crop residues contributed 65% of the total FRE, rice residues 18%, and corn residues 17%.

A distinct spatial pattern showing two main burning seasons can also been seen when FRE areal density is mapped (Fig. 6). During the summer burning season (May-June), most fires are located between 32°N - 36°N, extending from 112°E - 120°E near the coast. In the autumn season (Sept-Oct), less fire activity occurs than in the summer fire season and it is more evenly distributed across the entire study area, though there is still a focus of fire activity between 32 - 34°N and 112 - 119°E. Moreover, in the southwest of the study area (29 - 32°N and 112 - 114°E) we see a region that only appears to undergo substantial burning in the autumn. This is located in the centre of Hubei Province, which

287 contributes around 12% of the total rice yield of the whole of China (NBSC, 2015). This area contributes to between
288 10 and 18 % (year dependant) of the total autumn burning season FRE.

289

290 4.2 DMB Comparisons to GFAS and GFED

291 The outputs generated by our combined VIIRS and Himawari processing chain were compared to those of GFAS and
292 GFED4.1s (Fig. 7). Dry matter burned (DMB) was used as the common comparison metric, as this removes differences
293 arising from the use of different emissions factors within the inventories. Overall, the VIIRS-IM/Him DMB estimates
294 are around 2× to 5× higher than those reported for corresponding months by GFAS and GFED 4.1s. As detailed in
295 Zhang et al. (2017) and discussed in Section 2, VIIRS has the ability to detect far smaller (and lower FRP) fires than
296 MODIS, due to its far smaller pixel size and the fact that the I-band observations also retain their pixel area more
297 effectively across the swath. Ultimately, this difference results in far higher DMB being obtained by the VIIRS-
298 IM/Him inventory compared to the MODIS based GFAS and GFED inventories.

299 During the summer months of May-June, all three inventories (GFAS, GFED and VIIRS-IM/Himawari) show a clear
300 peak in DMB, but GFAS and VIIRS-IM/Him show a much sharper peak in June, while GFED's summer burning
301 season extends one month earlier (May) and later (July). This extended summer fire season reported by GFED is likely
302 the result false fire reporting, discussed at length in Zhang et al (2018). VIIRS-IM/Him shows a June DMB peak
303 ranging from 3.30 to 11.2 Tg, 2× higher than GFED4.1s (1.89 - 5.34 Tg) and GFAS (2.00 to 4.30 Tg). It should be
304 remembered that the conversion of daily average FRP to DMB in GFAS is derived via a calibration to GFED4.1s
305 (Kaiser *et al.*, 2012), so these two emissions databases understandably report similar monthly DMB totals.

306 For the autumn (Sept-Oct) burning season, the peaks in the GFAS and GFED inventories are much less pronounced
307 than the summer burning season peaks (Fig. 7). DMB in October ranges from 0.57 - 1.74 Tg for GFED, significantly
308 higher than the 0.31 - 0.61 Tg reported by GFAS, but far lower than the 1.62 - 3.05 Tg of the VIIRS-IM/Him inventory.
309 The VIIRS-IM/Him derived DMB estimates for eastern China are thus 2 to 3× higher than GFED4.1s and 5× higher
310 than GFAS; these represent larger differences than exist for the earlier summer burning season. This indicates that
311 agricultural fires burning during the autumn fire season may be on average smaller and/or more isolated from other
312 fires than they are in the summer burning season, and thus are even more likely to be missed by the MODIS AF
313 detection product (Giglio *et al.,* 2006) and/or the MODIS BA product (Giglio *et al.,* 2013) than they are during other
314 more intense burning periods.

315

316 4.3 Agricultural Fire Emissions Intercomparison

317 This section presents a comparison of the total annual agricultural fire emissions calculated using the VIIRS-IM/Him
318 method with other inventories of Chinese agricultural fire emissions in the literature, and against emissions totals from
319 other sectors to gain a better understanding of the relative importance of agricultural fire emissions. To compare with

320 other reported agricultural fire emission inventories for China, the DMB estimates produced herein were converted to

321 fire emissions estimates using the emissions factors and methods described in Section 3.3; these results are summarised

322 in Fig. 8 and Table 2.

323 From Fig. 8, it is clear that wheat residue burning is the primary agricultural emission source, accounting for over 50%

324 of the total emissions released each year (specifically 55-69% of $PM_{2.5}$, 71-81% of BC, 66-77% of CO_2, and 69-80%

325 of CO). Fig. 8 also indicates a considerable reduction in emissions in 2015 compared to previous years, largely

326 attributable to a reduction in the amount of wheat residue burnt. For example, total $PM_{2.5}$ emissions from agricultural

327 residue burning in eastern China for 2012-14 cover a relatively narrow range of 107 - 130 Gg (Fig. 8 & Table 2), but

328 decrease to 67 ± 24 Gg in 2015 due to an almost halving of DMB (Fig. 7); similar patterns are observed for BC, CO_2,

329 and CO (Fig.8).

330 From Table 2, it is apparent that emissions totals calculated using the VIIRS-IM/Him approach are consistently higher

331 than those reported by GFAS by factor of 1.2-4.2 (species/year dependent). Similarly, VIIRS-IM/Him emissions totals

332 for CO_2 and PM2.5 are greater than those reported by GFED by a factor of 1.1-1.7. In both cases, this can be explained

333 by the tendency of MODIS to miss activity from small fires compared to VIIRS. VIIRS-IM/Him emissions for CO

334 and BC in 2015 are lower than those reported for GFED, which can be attributed to differences in the emissions factors

335 used between the approaches.

336 Emissions totals calculated using the VIIRS-IM/Him approach are smaller than those estimated by CYBA studies for

337 the East China/North China Plain regions (Zhang et al., 2008; Huang et al., 2012; Qiu et al., 2016) by a factor of 2-5.

338 It is possible that the much higher totals estimated from the CYBA based studies maybe due to the use of very high

339 residue burning ratios (B_i in Eq. 1) for corn and rice in particular. This finding is discussed further in Section 5.

340 Liu *et al.,* (2015) estimated total emissions in the North China Plain region (a similar area to the study area used in

341 this paper) using MODIS FRP-based calculations, and assumed a modified Gaussian function for the diurnal cycle to

342 generate the daily FRE estimates from which emissions were then derived. These estimates are much closer in

343 magnitude to the equivalent estimates calculated using the VIIRS-IM/Him method than those from the CYBA studies,

344 however 2013 & 2014 estimates by Liu et al. are consistently lower (by a factor of 0.3-0.9); again, we attribute this

345 difference to the fact that MODIS based methods capture less fire activity than our VIIRS-IM/Him approach.

346 Interestingly, Liu *et al.* (2015) estimated far higher emission totals for 2012 compared to 2013 & 2014 and report

347 greater total CO and BC emissions than we do. For example, annual CO_2 emissions in 2012 (26,000 Gg) are > 2× their

348 reported total emissions for 2013 (9800 Gg) and 2014 (13,000 Gg). However, Liu *et al.*'s processing approach did not

349 provide any adjustment for the impact of the MODIS 'bow-tie' scan geometry effect, which leads to duplicated AF

350 detections and this FRP towards the edge of the MODIS swath, and which was highlighted as significant issue for

351 FRP quantification by Freeborn *et al.* (2008) and Zhang et al. (2017). This is a particular problem in MODIS data

352 from the year 2012, where large amount of duplicated observations have been found towards edge of swath (Fig. S2).

353 This problem has been addressed in GFAS using a scan-angle dependent weighing factor for the MODIS FRP data

354   (Kaiser *et al.,* 2012), as described in Section 2.5, and GFAS' CO_2 emissions from 2012 are only 24% and 10% higher

355   than from 2013 and 2014 respectively, a much more modest increase compared to that reported in Liu *et al.* (2015).

356   Fig. 9 presents a comparison of agricultural emissions calculated using the VIIRS-IM/Him method with emissions

357   from non-biomass burning sources produced by Li et al. (2014) for a sub-area of eastern China (32-36º N, 112-122º

358   E) for the year 2013. We note that crop burning emissions are of relatively little significance when considered on an

359   annual basis; for all four species (CO_2, CO, $PM_{2.5}$, BC), contributions from agricultural residue burning range between

360   0.56% and 2.0% of total annual emissions, with the majority of emissions resulting from industry and residential

361   sources. However, in June when agricultural burning and emissions are at a maximum, residue burning contributes

362   8.1%, 18%, 22% and 20% of total monthly emissions for CO_2, CO, $PM_{2.5}$ and BC respectively, highlighting the strong

363   seasonal impact agricultural burning can have on the emission of species that affect both climate and air quality.

364

5. ANALYSIS AND DISCUSSION

366   5.1 Importance of Wheat Residue Burning

367   Findings in Section 4 (Fig. 5 & 8) indicate that a larger proportion of wheat residue than corn or rice residue is burnt,

368   for several reasons. First, the yields of these three crop types in Eastern China are relatively similar - in 2015 for

369   example, wheat yield was 10% lower than rice yield, and only 20% higher than corn (Table S1; NBSC, 2015). Second,

370   the dry matter production-to-residue ratio (R_i in Eqn. 1) of wheat is not higher than that of rice or corn (Table S2;

371   Wang and Zhang, 2008). Third, with the exception of black carbon, the emission factors for wheat residues are broadly

372   similar to or smaller than the corresponding rice and corn emission factors. It is unknown why a greater fraction of

373   wheat residue than corn and rice residue is burnt, however, it is possible that local management practices and/or

374   stakeholder priorities differ depending upon the residue type and time of year at which crops are harvested, ultimately

375   impacting the fate of these residues e.g. residues from certain crops maybe valuable as fertiliser (Huang et al., 2012),

376   animal feed or for domestic/local energy production (Chen et al., 2017; Liu et al., 2008).

377

378   5.2 Discovery of A Winter Burning Season

379   As detailed in Section 4.1, small peaks in our dry matter burned (DMB) time-series are apparent in November-

380   December of each year (grey shaded area shown in Fig. 5). Since no mention of such a winter burning season was

381   found in the literature (e.g. Chen *et al.,* 2017; Huang *et al.,* 2012; Zhang *et al.,* 2008), these winter peaks were initially

382   considered to be erroneous and likely caused by VIIRS AF false alarms that had failed to be excluded by the landcover

383   and/or persistent thermal anomaly masking detailed in Zhang et al., (2017). Furthermore, according to the crop rotation

384   map derived from the MIRCA2000 data (Fig. S1), there is no obvious harvesting of wheat, corn, or rice during the

385   winter in eastern China. However, close examination of the original VIIRS data and the VIIRS-IM FRP product

386   generated from it by Zhang et al., (2017) shows that most of the AF pixels detected in eastern China in winter are in

387   fact located in or very close to areas classified as agricultural land (Fig. S3), and are not located close to industrial

388   areas of the type known to cause false AF detections (Zhang et al., 2017), nor do the AF detections appear multiple
389   times in the same month at the same location, as would be expected if they were false alarms generated by non-fire
390   features. It therefore seems highly probable that these AF detections are actually a consequence of true agricultural
391   burning (Fig. S3-5).

392   The most reasonable explanation for the winter AFs appears to be that some of the crop residues from the Sept-Oct
393   (Autumn) harvest season were left idle for a few months and burned in the winter, rather than immediately. Local
394   newspapers, online media and other information sources were consulted, and were found to support the existence of
395   winter residue burning episodes. One example is a report by Jiangsu Province TV station in 5 December 2013, where
396   a huge crop residue burning episode was reported in Hongze (Jiangsu Province), close to the location shown in Fig.
397   S3. Stills from this TV report show flames, thick smoke and extremely poor visibility resulting from the crop residue
398   burning, described in Chinese language subtitles (Fig. S4). Reports of similar episodes were found in different
399   websites/newspapers from across much of eastern China (e.g. Wang and Zhang, 2016; Za, 2015; Zuo, 2015).
400   Subsequent to this confirmation, an explanation as to why this activity may have occurred outside of the normal
401   burning season was sought. According to Yun Xia, a local governor of the Environmental Department in Hefei
402   (interview conducted by Anhui News; Zuo, 2015), the prohibition on agricultural burning started at beginning of
403   September in that area, and continued up until the 20th November. During this period, the local government strongly
404   enforced its polices aiming to restrict agricultural residue burning, and established almost continuous patrols to
405   identify areas likely to host crop residue fires in order to prevent their ignition. However, without a widespread and
406   cost-effective alternative way to dispose of their crop residues, local farmers may simply have stored the residue
407   material and burned it soon after the end of the prohibition period, when the intensive patrol period had ceased. The
408   end of the prohibition period coincides almost exactly with the time of the new winter burning season identified by
409   our VIIRS-IM/Him dataset (Figs. 5- 7).

410   The winter season is important for biomass burning in this area of China, accounting for between 19 and 36 % (year
411   dependant) of the combined autumn and winter FRE total. Based on the crop rotation map (Fig S1), this fire activity
412   was assigned to the burning of both corn and rice residues, with the contribution of each residue to total FRE (and
413   thus DMB) almost equal (49 % and 51 %, average over all years). This split by residue type is very similar to that
414   observed in the Autumn burning season (corn = 54 %, rice = 46 %, average over all years), despite the observed
415   variation in the spatial distribution of fire between autumn and winter (Fig. 6). In general, winter burning appears to
416   take place closer to provincial capitals than autumn burning does; the reason for this spatial shift in fire is discussed
417   in Section 5.4.

418

419   5.3 Disagreement Between Satellite Derived Emissions and Crop Yield Based Approaches

420   In Section 4.3, it was noted that annual emissions totals calculated using crop yield based approaches (CYBAs) are
421   greater than those calculated using the VIIRS-IM/Him method by a factor of 2-3, depending on species. We believe
422   that this discrepancy relates to the 'burning ratio' (BR) used in CYBA to produce emissions estimates. The burning

423   ratio is the ratio of crop residue burned in the field compared to the total amount of residue produced by harvesting,

424   and is a key parameter in bottom up CYBAs (see Eqn. 1, and Chen *et al.,* 2017; Gao *et al.,* 2002; Huang *et al.,* 2012;

425   Li *et al.,* 2016). Streets *et al.* (2003) used a uniform BR of 17 % derived from 1970's data, however more recent

426   studies often make use of regionally varying fractions. We identified three sources of regionally varying burning ratios

427   that are widely used in the CYBA literature:

428   i)   Wang and Zhang (2008), divided all provinces in China into six zones according to their geographical

429   distribution. A questionnaire-based survey conducted amongst farmers within these regions was used to

430   elucidate the level of burning activity, and using the responses it was determined that burning ratios for

431   the different categories ranged from 11% to 33%. Outputs were applied and referenced in a series of fire

432   emission studies (He *et al.,* 2011, Qin and Xie 2011, Zhang *et al.,* 2016).

433   ii)   Gao *et al.* (2002) derived a set of province-dependent burning ratios adopted from a large-scale

434   investigation of crop residue use across different Chinese provinces. These ratios have been used and

435   referenced in Huang *et al.* (2012), Yan *et al.* (2006), Zhang *et al.* (2008), and are shown in Fig. 10.

436   iii)   A derived value based on farmers' income levels, based on the fact that Cao *et al.,* (2006) found a positive

437   linear correlation between the income of farmers and burning ratio ($r = 0.81$). This relationship has been

438   applied within several fire emission studies (Sun *et al.,* 2016, Zhao *et al.,* 2015) and will be examined in

439   Section 5.4.

440   Using crop yield information and the DMB data derived from the VIIRS-IM/Him processing performed herein, it is

441   straight forward to reverse the CYBA methodology to calculate the burning ratio for each crop type. This procedure

442   can help confirm whether the outputs derived herein are comparable with those of the existing literature, as well as

443   enabling the advantages offered by the remote sensing time series to be fully exploited. The burning ratios (B_{ij}) for

444   each province *i* and crop type *j* are calculated from:

445     $B_{ij} = \frac{DMB_{ij}}{P_{ij}R_i C}$ (10)

446   Where DMB_{ij} is the estimated VIIRS DMB (g/m^2) for province *j* and crop *i*; P_{ij} is the yield of crop *i* for province *j* (kg);

447   R_i is the dry matter production-to-residue ratio for crop *i* (unitless) and *C* is crop combustion completeness (proportion,

448   0-1). The province level crop yield P_{ij} is derived from annually published statistical reports, and are presented in Table

449   S1. R_i and *C* are from Huang et al., (2012); and are presented in Table S2.

450   The crop and province dependent burning ratios calculated from the VIIRS-IM/Him data are shown in Fig. 10,

451   alongside the burning ratios from Gao *et al.* (2002). Fig. 10 indicates that there is considerable variation in burning

452   ratios between individual provinces, and that VIIRS-IM/Him wheat burning ratios for are clearly much higher than

453   rice/corn burning ratios. When averaged over the entire Eastern China study area, yearly mean burning ratios from

454   our results for wheat are highest (7.8 - 12%), followed by corn (1.7 - 2.3%), then rice (0.9 - 2.0%). Equivalent mean

455   burning ratios calculated using data from Gao *et al.* (2002) are 9.8 %, 5.9 % and 8.5 %, respectively. While VIIRS-

456   IM/Him wheat residue burning ratios are in reasonable agreement with those used in the various CYBA studies, our

457   rice and corn burning ratios are much lower; this appears to explain why total annual emissions from the VIIRS-
458   IM/Him approach are much lower than the total emissions obtained from the CYBA studies.

459   Fig. 10 also indicates that burning ratios are not only influenced by crop type and province, but also vary considerably
460   from year to year. For example, in 2012, satellite derived wheat burning ratios for the important agricultural provinces
461   of Anhui (30%), Shandong (11%), Jiangsu (24%) and Henan (11%) are not dissimilar to corresponding ratios (20%,
462   8%, 10%, 7% respectively) from Gao *et al.,* (2002). However, during 2015, values derived in this study are much
463   lower (Anhui = 6 %; Shandong = 4 %; Jiangsu = 4 %; Henan = 6 %). This interannual variation may be linked with
464   changing local farming activity and prohibition policies (Chen *et al.,* 2017, Li *et al.,* 2016, Yang *et al.,* 2008).

465   We believe that the disagreement between the burning ratios derived here and those used in CYBA derived studies
466   indicate that emissions inventories derived using traditional CYBAs may be overestimating agricultural burning
467   emissions, for two main reasons: (1) there appears to be considerable uncertainty and subjectivity associated with the
468   methods used to estimating burning ratios used in CYBA studies, and (2) many burning ratios used in CYBA studies
469   are taken from relatively old (>5-10 years) sources of data. For example, Street *et al.* (2003) use data from 1970's,
470   while most recent researchers use burning ratios from Wang and Zhang (2008) and Gao *et al.* (2002) as listed above
471   in this section.

472   As shown by this analysis, burning ratios appear to be subject to high spatial and interannual variability due to rapidly
473   changing agricultural policies and decision making that influences the fate of crop residues. As such, in order to ensure
474   reliable emissions estimates, we suggest that future agricultural emission studies and inventories that are based upon
475   CYBAs should endeavour to use burning ratios derived from data (1) with high granularity, and (2) that was collected
476   in the corresponding inventory year.

477

478   5.4 Influence of Social Factors on Agricultural Burning

479   As highlighted in Section 5.2, some studies assume a positive relationship between burning ratio and the mean local
480   income of farmers (Cao *et al.,* 2006; Qin and Xie, 2011). The explanation for this is that higher income areas have
481   better access to electricity and other energy sources, and thus have less need to utilise crop residues for heating and
482   cooking – leading to higher ratios of open burning at these locations. However, this is not what we observe in from
483   analyses carried out for this study. In Fig. 11a, minimal correlation was found between GDP and burning ratio, and
484   there is some suggestion of an inverse relationship between these variables (y=-89x+9542, r^2=0.13). When directly
485   comparing GDP with DMB, as Fig. 12 demonstrates, the provinces with the highest average annual DMB per m^2
486   (Anhui and Henan; 46 and 27 $g.m^{-2}.yr^{-1}$ respectively) have lower GDP values (US$ 5,580 and 5,335 per capita) than
487   provinces with lower annual DMB densities (e.g. Shandong and Jiangsu, with 15 and 21 $g.m^{-2}.yr^{-1}$ respectively) but
488   high GDP per capita (USD$ 9,882 and 13,311 respectively). In fact, across the eastern China study area, our annual
489   total DMB metric was found to be somewhat inversely correlated with GDP per capita ($r^2 = 0.33$; Fig. 11b).

490   We theorise that the observed inverse correlation between GDP and DMB results from the fact that alternative residue

491   disposal methods to biomass burning have a relatively high cost, and can only be afforded by wealthier

492   farmers/provinces. For example, the local government of Jiangsu Province (a relatively wealthy province [$ 13,311

493   per capita] with only moderate DMB [21 $g.m^{-2}.yr^{-1}$]) released a regulation in 2009 stating that by the end of 2012, over

494   35% of crop residues should been incorporated into the soil after mechanised harvesting. The regulation also indicated

495   that the local government should include a budget for improving the efficiency of agricultural machinery and subsidise

496   farmers who follow this regulation. Furthermore, alternative uses for crop residues are often expensive, and are likely

497   only a viable option in relatively wealthy areas. For example, research on residue burning for power generation shows

498   the government needs to pay at least 20% of the total cost of the operation to keep the power plants running, partly

499   because of the high costs associated with residue collection and transportation from the fields (Li and Hu, 2009).

500   In addition to influencing the quantity of material burned and when it is burned, societal factors also appear influence

501   the spatial pattern of burning within provinces, and at more granular levels such as at the 0.1° grid cell level. The work

502   presented in Section 5.1 suggests that the winter burning season (Nov-Dec) is caused by delayed burning of residues

503   left over from the autumn harvest season, because of prohibition policies related to burning being more robustly

504   enforced earlier in the season. Fig. 6 also showed that the spatial distribution of FRE areal density during winter is

505   different from the normal autumn burning season that occurs in Sep-Oct. Generally, the areas of strongest burning are

506   further from the provincial capital cities (marked by the green stars in Fig. 6) during autumn. For example, fires in

507   Anhui Province are mainly distributed in the north during autumn, whilst fire locations change to the south (closer to

508   the capital city of Hefei) during the delayed winter burns. A similar example can also be seen in Hubei Province,

509   where fires shift from west to east from the autumn to winter burning seasons.

510   To examine this in a more quantitative manner, we calculated the distance from each grid cell shown in Fig. 6 to their

511   provincial capitals. Fig. 13 shows the normalised frequency distribution of the distance from the capital to the top 10%

512   of FRE releasing grid cells in each province, using data from the four burning seasons during the 2012-2015 period.

513   The first and third distance quartiles during the autumn season are 109 km and 214 km respectively, but for the 'lagged'

514   winter burning season, the distribution shifts to far shorter distances (first and third quartiles of 70 km and 153 km

515   respectively). Similarly, the mean distance from provincial capitals also decreased from 165 km in autumn to 124 km

516   in winter. A Kolmogorov–Smirnov (K-S) test was performed to evaluate the difference between the distributions of

517   distance data for the autumn and winter burning seasons, and the resulting high K-S statistic ($0.30, p < 0.001$) indicates

518   that the distribution of distances during the winter months is substantially different to the autumn distance distribution.

519   Similar results were found when we applied the K-S test to each calendar year of data separately (not shown). One

520   possible explanation for this observed difference is that the geographical shift might also be linked with the policies

521   aimed at prohibiting burning, since areas close to capital cities are likely to have more resources for enforcing the

522   prohibition compared to areas more distant from the major urban populations.

523

524

6. SUMMARY AND CONCLUSION

We have developed a new state-of-the-art agricultural burning emissions inventory ('VIIRS-IM/Him') for eastern China by combining fire radiative power (FRP) observations from the VIIRS and Himawari-8 sensors for the 2012-2015 period. While several other studies have also used satellite EO data to develop such inventories, they have all relied on MODIS fire products for their source observations. Such inventories include the global GFED and GFAS inventories, several Chinese regional studies (e.g. Huang et al., 2012, Liu et al., 2015). MODIS fire products are known to show very high omission rates in environments dominated by small agricultural fires (Randerson et al., 2012; Zhang et al., 2017, 2018), but the 'small fire optimised' VIIRS-IM product of Zhang et al. (2017) used in this study detects far more of the fire activity across eastern China and on average show FRP totals around 4x higher than those of the MODIS AF products. To convert the twice-daily VIIRS-IM FRP product information to daily time-integrated FRE, we have used new diurnal fire cycle data from Himawari-8, a geostationary satellite positioned over east Asia that can best capture the specific diurnal fire variability of the agricultural burning regions.

Our final VIIRS/Him agricultural fire emissions inventory reports dry matter burned (DMB) totals around 2-5× higher than is reported by GFAS and GFED 4.1s in eastern China for corresponding time periods. Use of a crop rotation map allowed our VIIRS-IM/Him fire and emissions outputs to be disaggregated by individual crop types, and we found wheat residue burning to be the primary agricultural emission source, accounting for over 50% of the total emissions each year for all investigated smoke constituents (CO_2, CO, $PM_{2.5}$ and black carbon). A strong seasonal variation in fire activity and emissions is seen, with annual peak activity occurring in summer (May-June) as a result of wheat residue burning, and a smaller secondary activity peak occurring in autumn (Sept-Oct) as a result of corn and rice residue burning. Furthermore, we discovered a new winter (Nov-Dec) agricultural residue burning season. As no crop harvesting occurs during winter, we suspect that this fire activity results from farmers burning previously stored residues from the autumn harvest in winter, after autumn residue burning prohibitions have been lifted. This theory is supported by our observation of statistically distinct spatial burning patterns in the autumn and winter seasons; the majority of autumn burning occurs at a greater distance from provincial capitals than the winter burning does. This may reflect stronger enforcement of autumn residue burning prohibition measures in close proximity to major urban population centres than in rural locations. Farmers in areas with stronger prohibition enforcement (typically closer to urban areas) then burn their agricultural residue in winter.

Detailed comparison to existing inventories showed that our VIIRS-IM/Him annual emissions totals are 1.2-4.7× greater than those reported by GFAS, and 0.5-1.7x those reported by GFED4.1s, with some inter-species variability due to the use of different emissions factors between the inventories. By contrast, the VIIRS-IM/Him inventory shows emissions totals that are on average lower than those from emission inventories derived using crop yield based approaches (CYBA) by a factor of 2-5x. This discrepancy is believed to be primarily due to many CYBAs using outdated and/or inappropriate burning ratios, that consequently leads to CYBAs overestimating the amount of crop residue DMB annually. Back calculated burning ratios from the VIIRS-IM/Him data suggest that burning ratios for rice and corn are much lower than the CYBA literature suggests (approx. 0.9-2.3 % rather than 11-33 %). We also noted considerable inter-provincial and interannual variation in these back calculated burning ratios, for example,

561 wheat burning ratios significantly decrease over our four-year study period. This strongly suggests that high spatial

562 resolution, up-to-date burning ratios should always be used in CYBA for agricultural burning fire emission estimation.

563 Furthermore, several CYBA approaches (e.g. Sun *et al.,* 2016, Zhao *et al.,* 2015) have derived burning ratios from

564 provincial GDP data, assuming a positive relationship between these variables (Cao *et al.,* 2006). However, we found

565 evidence of an opposite (i.e. negative) relationship between provincial GDP and the amount of DMB in agricultural

566 fires, hypothesised to be due to the higher cost of disposal of crop residues by non-biomass burning methods. This

567 suggests that great care needs to be taken when deriving burning ratios for use in future agricultural emissions

568 inventories based upon CYBA methods, and that satellite remote sensing approaches based on EO datasets that

569 adequately detect the presence of agricultural fires are a far better approach to fire emissions estimation in such

570 environments.

571

572

573 **ACKNOWLEDGEMENTS**

574 This work has been supported by the NERC National Centre for Earth Observation (NE/R000115/1) and specifically

575 by NERC Grant NE/M017729/1. The Natural Environment Research Council (NERC) provides national capability

576 funding for NCEO, and this work is an output of nceo020005 and NERC Grant NE/S014004/1. We thank the

577 Leverhulme Trust for their support of the Leverhulme Centre for Wildfires, Environment and Society. We

578 acknowledge the National Natural Science Foundation of China (No. 41775162) who funded L. Wang. The VIIRS

579 SDR and MODIS data were retrieved from CLASS and Reverb, and are courtesy of the NASA EOSDIS LP DAAC

580 and USGS EROS Centre, South Dakota. GFAS data was generated using Copernicus Atmosphere Monitoring Service

581 Information, operated by ECMWF. All data storage and processing were conducted using the UK's JASMIN super-

582 data-cluster system, managed by UK STFC's Centre for Environmental Data Analysis (CEDA).

583

584 **REFERENCES**

585 Andela, N., Kaiser, J.W., Van der Werf, G.R. and Wooster, M.J., 2015. New fire diurnal cycle characterizations to improve fire
586   radiative energy assessments made from MODIS observations. Atmospheric Chemistry and Physics, 15(15), pp.8831-8846.
587 Andreae, M. O. & Merlet, P. 2001. Emission of trace gases and aerosols from biomass burning. Global biogeochemical cycles,
588   15(4), pp 955-966.
589 Bond, T. C., Doherty, S. J., Fahey, D., Forster, P., Berntsen, T., DeAngelo, B., Flanner, M., Ghan, S., Kärcher, B. & Koch, D. 2013.
590   Bounding the role of black carbon in the climate system: A scientific assessment. Journal of Geophysical Research:
591   Atmospheres, 118(11), pp 5380-5552.
592 Cao, G., Zhang, X. & Zheng, F. 2006. Inventory of black carbon and organic carbon emissions from China. Atmospheric
593   Environment, 40(34), pp 6516-6527.
594 Chan, C. K. & Yao, X. 2008. Air pollution in mega cities in China. Atmospheric Environment, 42(1), pp 1-42.
595 Cheng, Y., Engling, G., He, K. B., Duan, F. K., Ma, Y. L., Du, Z. Y., Liu, J. M., Zheng, M. & Weber, R. J. 2013. Biomass burning
596   contribution to Beijing aerosol. Atmos. Chem. Phys., 13(15), pp 7765-7781.
597 Chen, J., Chen, J., Liao, A., Cao, X., Chen, L., Chen, X., He, C., Han, G., Peng, S., Lu, M., Zhang, W., Tong, X., Mills, J., 2015.
598   Global land cover mapping at 30m resolution: A POK-based operational approach. ISPRS J. Photogramm. Remote Sens.,
599   Global Land Cover Mapping and Monitoring 103, 7–27. https://doi.org/10.1016/j.isprsjprs.2014.09.002
600 Chen, J., Li, C., Ristovski, Z., Milic, A., Gu, Y., Islam, M.S., Wang, S., Hao, J., Zhang, H., He, C. and Guo, H., 2017. A review of
601   biomass burning: Emissions and impacts on air quality, health and climate in China. Science of the Total Environment.

602 Du, H., Kong, L., Cheng, T., Chen, J., Du, J., Li, L., Xia, X., Leng, C. & Huang, G. 2011. Insights into summertime haze pollution
603   events over Shanghai based on online water-soluble ionic composition of aerosols. Atmospheric Environment, 45(29), pp
604   5131-5137.
605 Ellicott, E., Vermote, E., Giglio, L. and Roberts, G., 2009. Estimating biomass consumed from fire using MODIS FRE. Geophysical
606   Research Letters, 36(13).
607 Freeborn, P. H., Wooster, M. J., Hao, W. M., Ryan, C. A., Nordgren, B. L., Baker, S. P. & Ichoku, C. 2008. Relationships between
608   energy release, fuel mass loss, and trace gas and aerosol emissions during laboratory biomass fires. Journal of Geophysical
609   Research: Atmospheres, 113(D1), pp D01301.
610 Fu, J. Y., Jiang, D., Huang, Y. H., 2014a. 1-km grid population dataset of China, Global Change Research Data
611   Publishing & Repository, DOI:10.3974/geodb.2014.01.06.V1
612 Fu, J. Y., Jiang, D., Huang, Y. H., 2014b. 1-km grid GDP dataset of China, Global Change Research Data Publishing
613   & Repository, DOI:10.3974/geodb.2014.01.07.V1Gao, X., Ma, W., Ma, C., Zhang, F., Wang, Y., 2002. Analysis of the
614   current status of utilization of crop straw in China. Journal of Huazhong Agricultural University 21, 242–247 (in Chinese).
615 Giglio, L., Csiszar, I. & Justice, C. 2006. Global distribution and seasonality of active fires as observed with the Terra and Aqua
616   Moderate Resolution Imaging Spectroradiometer (MODIS) sensors. J. Geophys. Res, 111(G02016.
617 Giglio, L., Randerson, J.T. and Werf, G.R., 2013. Analysis of daily, monthly, and annual burned area using the fourth-generation
618   global fire emissions database (GFED4). Journal of Geophysical Research: Biogeosciences, 118(1), pp.317-328.
619 Goldberg, M.D., Kilcoyne, H., Cikanek, H., Mehta, A., 2013. Joint Polar Satellite System: The United States next generation
620   civilian polar-orbiting environmental satellite system. J. Geophys. Res. Atmospheres 118, 13,463-13,475.
621   https://doi.org/10.1002/2013JD020389
622 He, M., Zheng, J., Yin, S. & Zhang, Y. 2011. Trends, temporal and spatial characteristics, and uncertainties in biomass burning
623   emissions in the Pearl River Delta, China. Atmospheric Environment, 45(24), pp 4051-4059.
624 Huang, X., Li, M., Li, J. & Song, Y. 2012. A high-resolution emission inventory of crop burning in fields in China based on MODIS
625   Thermal Anomalies/Fire products. Atmospheric Environment, 50(0), pp 9-15.
626 Jiang, D., Zhuang, D., Fu, J., Huang, Y. & Wen, K. 2012. Bioenergy potential from crop residues in China: Availability and
627   distribution. Renewable and Sustainable Energy Reviews, 16(3), pp 1377-1382.
628 Kaiser, J. W., Heil, A., Andreae, M. O., Benedetti, A., Chubarova, N., Jones, L., Morcrette, J. J., Razinger, M., Schultz, M. G.,
629   Suttie, M. & van der Werf, G. R. 2012. Biomass burning emissions estimated with a global fire assimilation system based
630   on observed fire radiative power. Biogeosciences, 9(1), pp 527-554.
631 Li, W., Shao, L. & Buseck, P. 2010. Haze types in Beijing and the influence of agricultural biomass burning. Atmospheric
632   Chemistry and Physics, 10(17), pp 8119-8130.
633 Li, J.F. and Hu, Y.S., 2009. Analysis on investment and operation of straw-fired power plants in Jiangsu province. Electric power
634   technologic economics, 5, p.005 (in Chinese).
635 Li, J., Li, Y., Bo, Y. and Xie, S., 2016. High-resolution historical emission inventories of crop residue burning in fields in China
636   for the period 1990–2013. Atmospheric Environment, 138, pp.152-161.
637 Li, M., Zhang, Q., Kurokawa, J.I., Woo, J.H., He, K.B., Lu, Z., Ohara, T., Song, Y., Streets, D.G., Carmichael, G.R. and Cheng,
638   Y.F., 2015. MIX: a mosaic Asian anthropogenic emission inventory for the MICS-Asia and the HTAP projects. Atmos.
639   Chem. Phys. Discuss, 15(23), pp.34813-34869.
640 Liu, M., Song, Y., Yao, H., Kang, Y., Li, M., Huang, X. and Hu, M., 2015. Estimating emissions from agricultural fires in the
641   North China Plain based on MODIS fire radiative power. Atmospheric environment, 112, pp.326-334.
642 Liu, H., Jiang, G. M., Zhuang, H. Y. & Wang, K. J. 2008. Distribution, utilization structure and potential of biomass resources in
643   rural China: With special references of crop residues. Renewable and Sustainable Energy Reviews, 12(5), pp 1402-1418.
644 NBSC (National Bureau of Statistic of China) China Statistical Yearbook, 480 2003–2015, China Statistics Press, Beijing (2004–
645   2016) (in Chinese).
646 Portmann, F. T., Siebert, S. & Döll, P. 2010. MIRCA2000—Global monthly irrigated and rainfed crop areas around the year 2000:
647   A new high-resolution data set for agricultural and hydrological modeling. Global Biogeochemical Cycles, 24(1).
648 Qin, Y. & Xie, S. D. 2011. Historical estimation of carbonaceous aerosol emissions from biomass open burning in China for the
649   period 1990–2005. Environmental Pollution, 159(12), pp 3316-3323.
650 Randerson, J., Chen, Y., Werf, G., Rogers, B. & Morton, D. 2012. Global burned area and biomass burning emissions from small
651   fires. Journal of Geophysical Research: Biogeosciences (2005–2012), 117(G4), pp.
652 Roberts, G., Wooster, M.J. and Lagoudakis, E., 2009. Annual and diurnal african biomass burning temporal dynamics.
653   Biogeosciences, 6(5), pp.849-866.
654 Roberts, G., Wooster, M.J., Xu, W., Freeborn, P.H., Morcrette, J.J., Jones, L., Benedetti, A. and Kaiser, J., 2015. LSA SAF Meteosat
655   FRP Products: Part 2--Evaluation and demonstration of use in the Copernicus Atmosphere Monitoring Service (CAMS).
656   Atmospheric Chemistry & Physics Discussions, 15(12).
657 Schroeder, W., Oliva, P., Giglio, L. and Csiszar, I.A., 2014. The New VIIRS 375 m active fire detection data product: Algorithm
658   description and initial assessment. Remote Sensing of Environment, 143, pp.85-96.
659 Streets, D.G., Yarber, K.F., Woo, J.H. and Carmichael, G.R., 2003. Biomass burning in Asia: Annual and seasonal estimates and
660   atmospheric emissions. Global Biogeochemical Cycles, 17(4).
661 Sun, J., Peng, H., Chen, J., Wang, X., Wei, M., Li, W., Yang, L., Zhang, Q., Wang, W. & Mellouki, A. 2016. An estimation of
662   CO2 emission via agricultural crop residue open field burning in China from 1996 to 2013. Journal of Cleaner Production,
663   112, Part 4(2625-2631.

van der Werf, G. R., Randerson, J. T., Giglio, L., Collatz, G. J., Mu, M., Kasibhatla, P. S., Morton, D. C., DeFries, R. S., Jin, Y. & van Leeuwen, T. T. 2010. Global fire emissions and the contribution of deforestation, savanna, forest, agricultural, and peat fires (1997–2009). Atmos. Chem. Phys., 10(23), pp 11707-11735.

van der Werf, G. R., Randerson, J. T., Giglio, L., van Leeuwen, T. T., Chen, Y., Rogers, B. M., Mu, M., van Marle, M. J. E., Morton, D. C., Collatz, G. J., Yokelson, R. J., and Kasibhatla, P. S.: Global fire emissions estimates during 1997–2016, Earth Syst. Sci. Data, 9, 697-720, https://doi.org/10.5194/essd-9-697-2017, 2017.

Wang & Zhang, 2016, http://news.chengdu.cn/2016/1106/1829718.shtml,Chengdu Business Daily

Wang, S. & Zhang, C. 2008. Spatial and temporal distribution of air pollutant emissions from open burning of crop residues in China. Sciencepaper online, 3(5), pp 329-333.

Wolfe, R.E., Lin, G., Nishihama, M., Tewari, K.P., Tilton, J.C. and Isaacman, A.R., 2013. Suomi NPP VIIRS prelaunch and on-orbit geometric calibration and characterization. Journal of Geophysical Research: Atmospheres, 118(20), pp.11-508.

Wooster, M. J., Roberts, G., Perry, G. L. W. & Kaufman, Y. J. 2005. Retrieval of biomass combustion rates and totals from fire radiative power observations: FRP derivation and calibration relationships between biomass consumption and fire radiative energy release. Journal of Geophysical Research: Atmospheres, 110(D24), pp D24311.

Xu, W., Wooster, M.J., Kaneko, T., He, J., Zhang, T. and Fisher, D., 2017. Major advances in geostationary fire radiative power (FRP) retrieval over Asia and Australia stemming from use of Himarawi-8 AHI. Remote Sensing of Environment, 193, pp.138-149.

Yamaji, K., Li, J., Uno, I., Kanaya, Y., Irie, H., Takigawa, M., Komazaki, Y., Pochanart, P., Liu, Y., Tanimoto, H., Ohara, T., Yan, X., Wang, Z. & Akimoto, H. 2010. Impact of open crop residual burning on air quality over Central Eastern China during the Mount Tai Experiment 2006 (MTX2006). Atmos. Chem. Phys., 10(15), pp 7353-7368.

Yan, X., Ohara, T. & Akimoto, H. 2006. Bottom-up estimate of biomass burning in mainland China. Atmospheric Environment, 40(27), pp 5262-5273.

Yang, S., He, H., Lu, S., Chen, D. & Zhu, J. 2008. Quantification of crop residue burning in the field and its influence on ambient air quality in Suqian, China. Atmospheric Environment, 42(9), pp 1961-1969.

Za, 2015, http://www.chinanews.com/sh/2015/11-04/7606112.shtml, Legislative Evening Newspaper

Zhang, H., Ye, X., Cheng, T., Chen, J., Yang, X., Wang, L. & Zhang, R. 2008. A laboratory study of agricultural crop residue combustion in China: Emission factors and emission inventory. Atmospheric Environment, 42(36), pp 8432-8441.

Zhang, L., Liu, Y. and Hao, L., 2016. Contributions of open crop straw burning emissions to PM2. 5 concentrations in China. Environmental Research Letters, 11(1), p.014014.

Zhang, T., Wooster, M.J., Green, D.C. and Main, B., 2015. New field-based agricultural biomass burning trace gas, PM2. 5, and black carbon emission ratios and factors measured in situ at crop residue fires in Eastern China. Atmospheric Environment, 121, pp.22-34.

Zhang, T., Wooster, M.J. and Xu, W., 2017. Approaches for synergistically exploiting VIIRS I-and M-Band data in regional active fire detection and FRP assessment: A demonstration with respect to agricultural residue burning in Eastern China. Remote sensing of environment, 198, pp.407-424.

Zhang, T., Wooster, M., de Jong, M. and Xu, W., 2018. How Well Does the 'Small Fire Boost'Methodology Used within the GFED4. 1s Fire Emissions Database Represent the Timing, Location and Magnitude of Agricultural Burning?. Remote Sensing, 10(6), p.823.

Zhao, H., Tong, D. Q., Gao, C. & Wang, G. 2015. Effect of dramatic land use change on gaseous pollutant emissions from biomass burning in North Eastern China. Atmospheric Research, 153(429-436).

Zhou, L., Divakarla, M., Liu, X., Layns, A., Goldberg, M., 2019. An Overview of the Science Performances and Calibration/Validation of Joint Polar Satellite System Operational Products. Remote Sens. 11, 698. https://doi.org/10.3390/rs11060698

Zuo 2015, http://www.chinanews.com/gn/2015/12-11/7666514.shtml, Anhui News

709 **Table 1:** Emission Factors for agricultural residue burning used in this study. Wheat and rice emission factors were
710 derived from field measurements conducted in eastern China and reported by Zhang et al. (2015), while the corn
711 emission factors are from Andreae and Merlet (2001), the same as those used in GFAS (Kaiser *et al.,* 2012). *$PM_{2.5}$
712 = particulate matter with diameter < 2.5μm
713

| | Emissions Factor (g.kg^{-1}) | | |
	Wheat	Corn	Rice
CO_2	1739±19	1308±14	1761±30
CO	60±12	92±18	47±19
$PM_{2.5}$*	6.1±1.3	8.3±1.8	9.6±4.3
Black Carbon	0.70±0.09	0.42±0.05	0.56±0.04

714
715 **Table 2:** Total species-specific fire emissions calculated in this study for agricultural burning in eastern China, and
716 comparison to those contained within other fire emissions inventories and calculated in previous studies.
717

| Reference | Region | Year | Method | Emissions (Gg.yr^{-1}) | | | |
				CO_2	CO	$PM_{2.5}$	BC
This study	Eastern China	2012	Satellite	31066 ± 1960	1035±327	124±43	11±1.8
		2013		31107 ± 1748	1025±320	130±44	11±1.7
		2014		27069 ± 1421	904±279	107±36	10±1.5
		2015		16932 ± 1044	562±177	70±24	6±0.95
GFAS	Eastern China	2012	Satellite	9219	649	58	3.0
Kaiser *et al.,* 2012		2013		8173	576	52	2.6
		2014		8760	617	55	2.8
		2015		6818	480	43	2.2
GFED4.1s	Eastern China	2012	Satellite	18629	1199	74	8.8
Van der Werf *et al*., 2017		2013		24034	1547	95	11
		2014		18241	1173	72	8.6
		2015		15892	1023	63	7.5
Liu *et al.,* 2015	NCP[1]	2012	Satellite	26000	1700	102	13
		2013		9800	630	39	5
		2014		13000	820	50	6
Zhang et al., 2008	Eastern China[3]	2004	CYBA[2]	67703	5624	-	-
Huang et al., 2012	Eastern China[3]	2006	CYBA	41374	2668	164	20
Qiu et al., 2016	Eastern China	2013	CYBA	72071	2549	445	42
Li et al., 2016	NCP	2012	CYBA	68675	5983	452	23
Sun et al., 2016	China	2013	CYBA	192540	-	-	-
Street *et al.,* 2003	China	2000	CYBA	160000	10000	-	70
Yan *et al.,* 2006	China	2000	CYBA	184000	11000	470	80

718 [1] NCP refers to the North China Plain, which has a geographic extent similar to that of this study (32-41ºN, 113-121ºE).
719 [2] CYBA refers to Crop Yield Based Approaches, see Section 2.6.1
720 [3] Sum of provinces/cities shown in Fig.1 of this study.
721
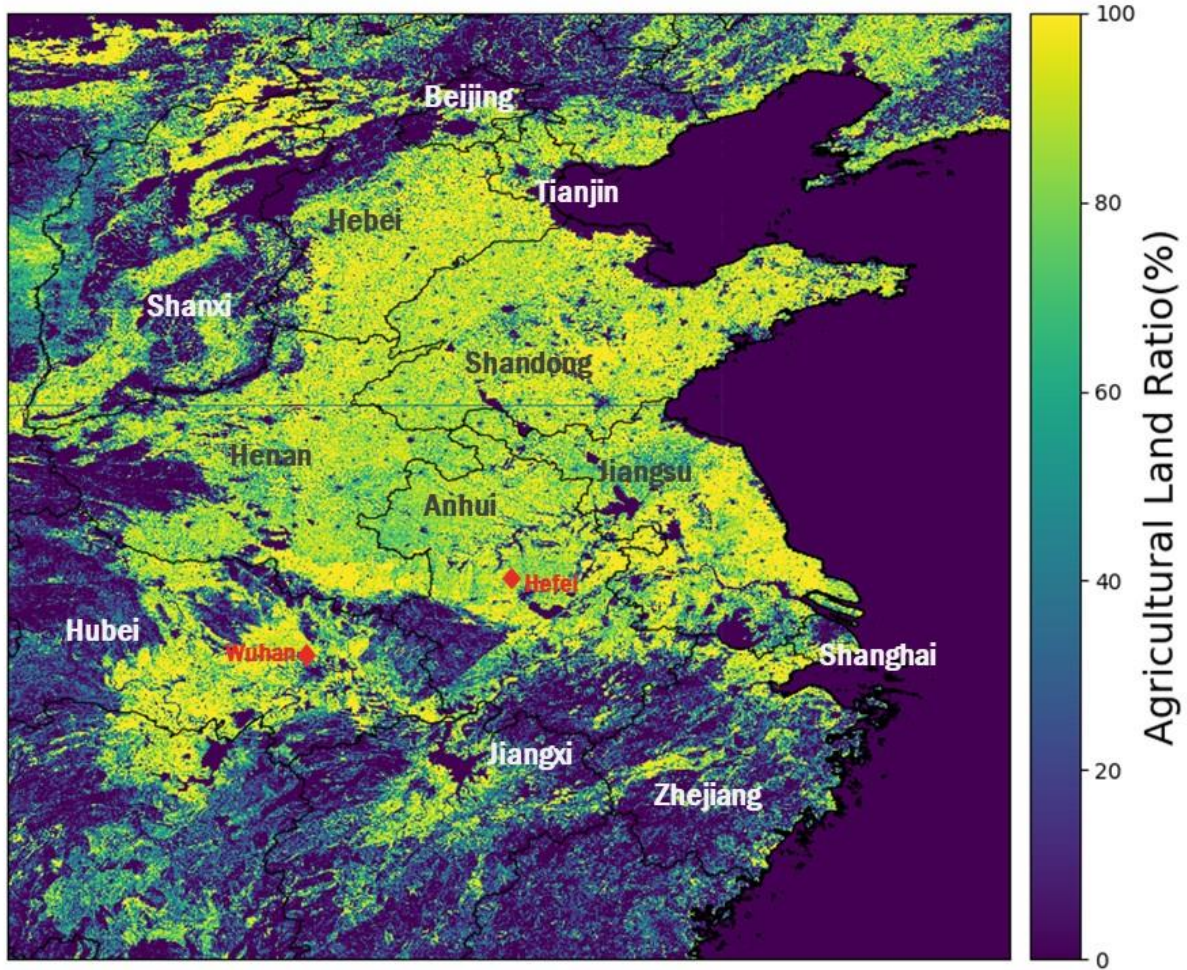
722
723 **Figure 1:** The spatial extent of the study area (111-123° E, 27-40° N). The agricultural land ratio taken from the
724 GlobeLand30 land cover product (Chen et al, 2015) was re-gridded to 0.01 degree spatial resolution, and is overlain
725 with the main provinces, mega-cities and some important provincial capital cities in eastern China. The basic layer of
726 country/province borders within this map was created using Python Basemap library.
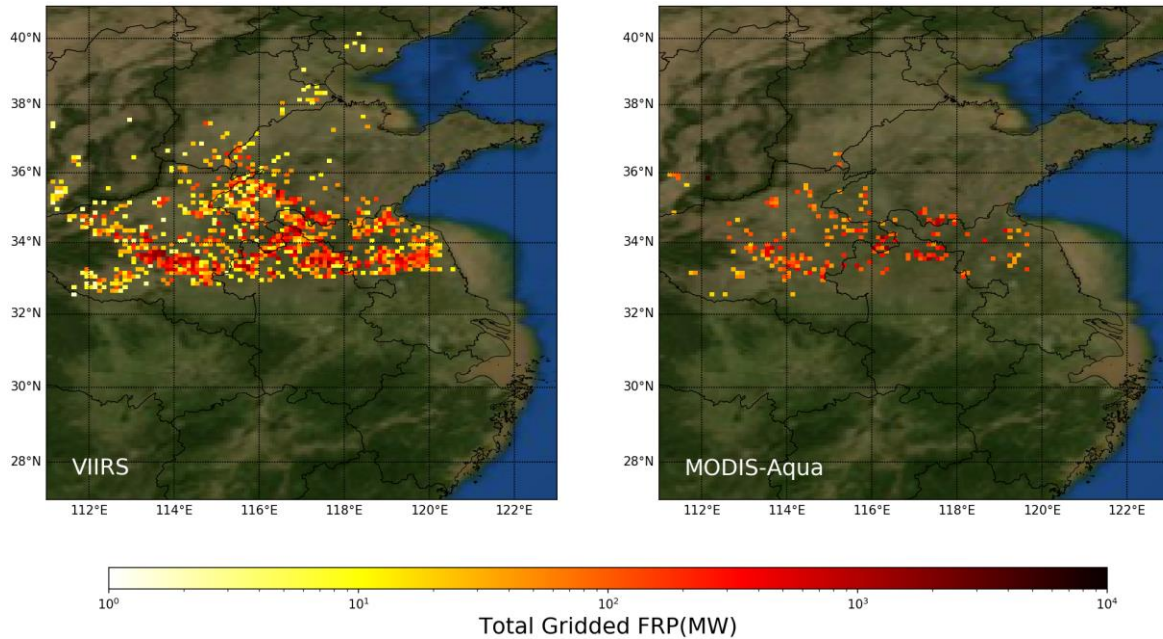
727
728 **Figure 2:** Example of the spatial distribution of total gridded FRP (MW; calculated per 0.1° grid cell) calculated from
729 near simultaneous VIIRS-IM and MODIS Aqua data collected over the eastern China study area of Fig. 1 on June
730 12th, 2012. The VIIRS-IM data product clearly quantifies a higher proportion of the FRP from fires burning in the
731 region at the time of the satellite overpass than MODIS Aqua does. The basic layer of country/province borders within
732 this map was created using Python Basemap library.
733
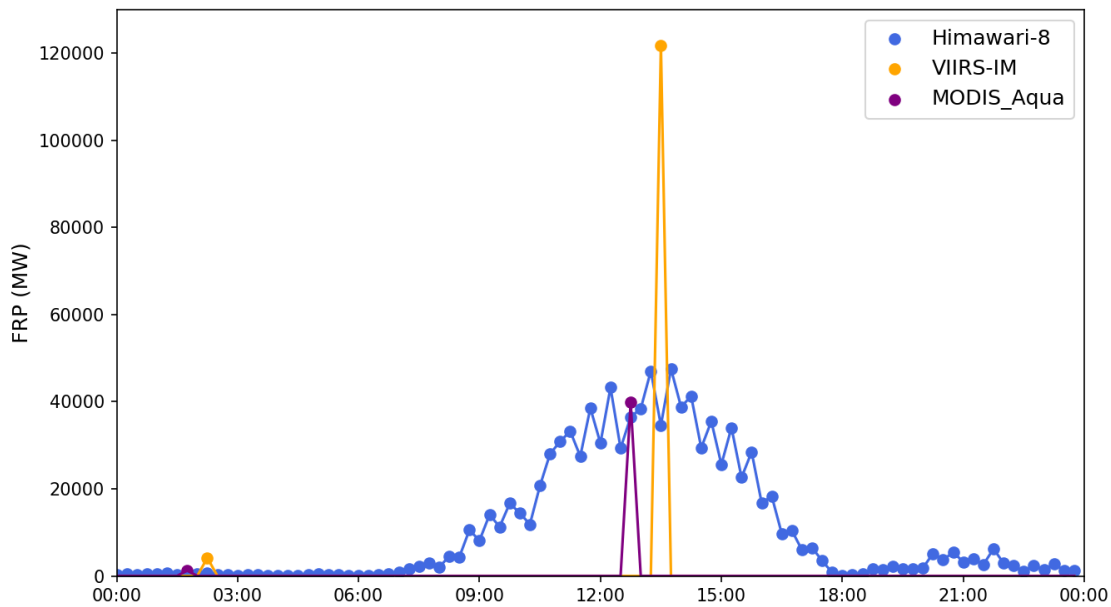
734
735 **Figure 3:** Time series of spatially summed FRP for eastern China, as retrieved from geostationary Himawari, and
736 polar-orbiting VIIRS-IM and MODIS observations made on June 11th, 2015. VIIRS and MODIS Aqua provide
737 typically two observations per day, and sometimes three when the swath overlaps from different orbits occur.
738 Himawari provides 144 observations per day.
739
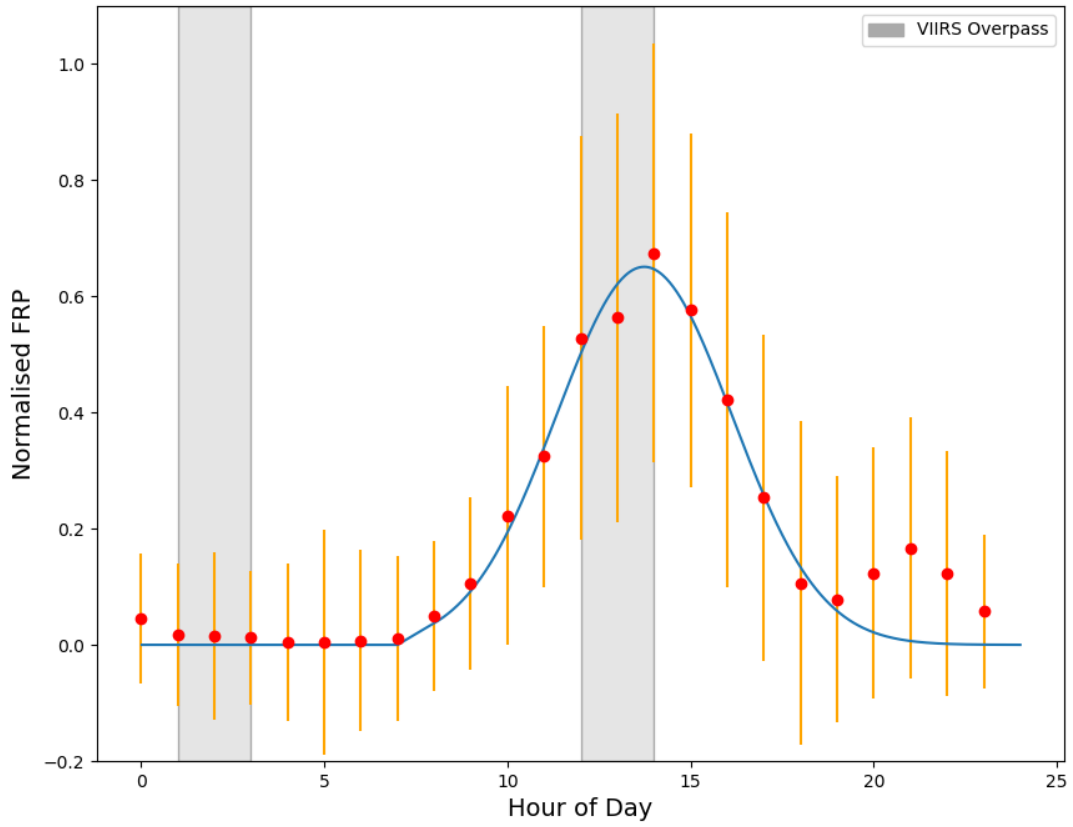
740
741 **Figure 4:** Time series of hourly normalised fire radiative power derived from Himawari-8 FRP data generated using
742 the algorithm of Xu et al. (2017) over eastern China at 0.1 degree for June 2015 (the 'Summer' diurnal fire cycle).
743 The blue curve shows the best fit of the Gaussian distribution, with orange error bar show standard deviation. Grey
744 shading shows the two daily VIIRS overpass periods.
745
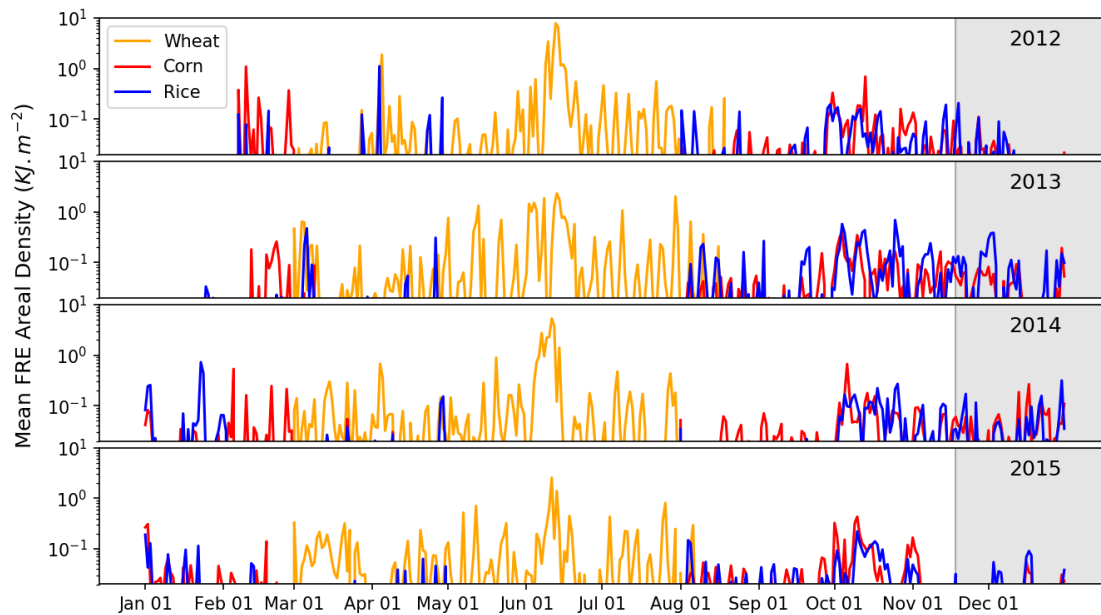
746
747 **Figure 5:** Time-series of mean daily FRE areal density (kJ m^{-2}, calculated per 0.1° grid cell) from 2012-2015 for the
748 entire study area disaggregated by crop residue type (wheat, corn and rice) according to the method described in
749 Section 2.4. Grey shaded areas highlighted the usual newly discovered winter burning season from mid-November to
750 December when no crop harvesting occurs but where fires are clearly occurring. This period of agricultural burning
751 is discussed further in Section 5.1
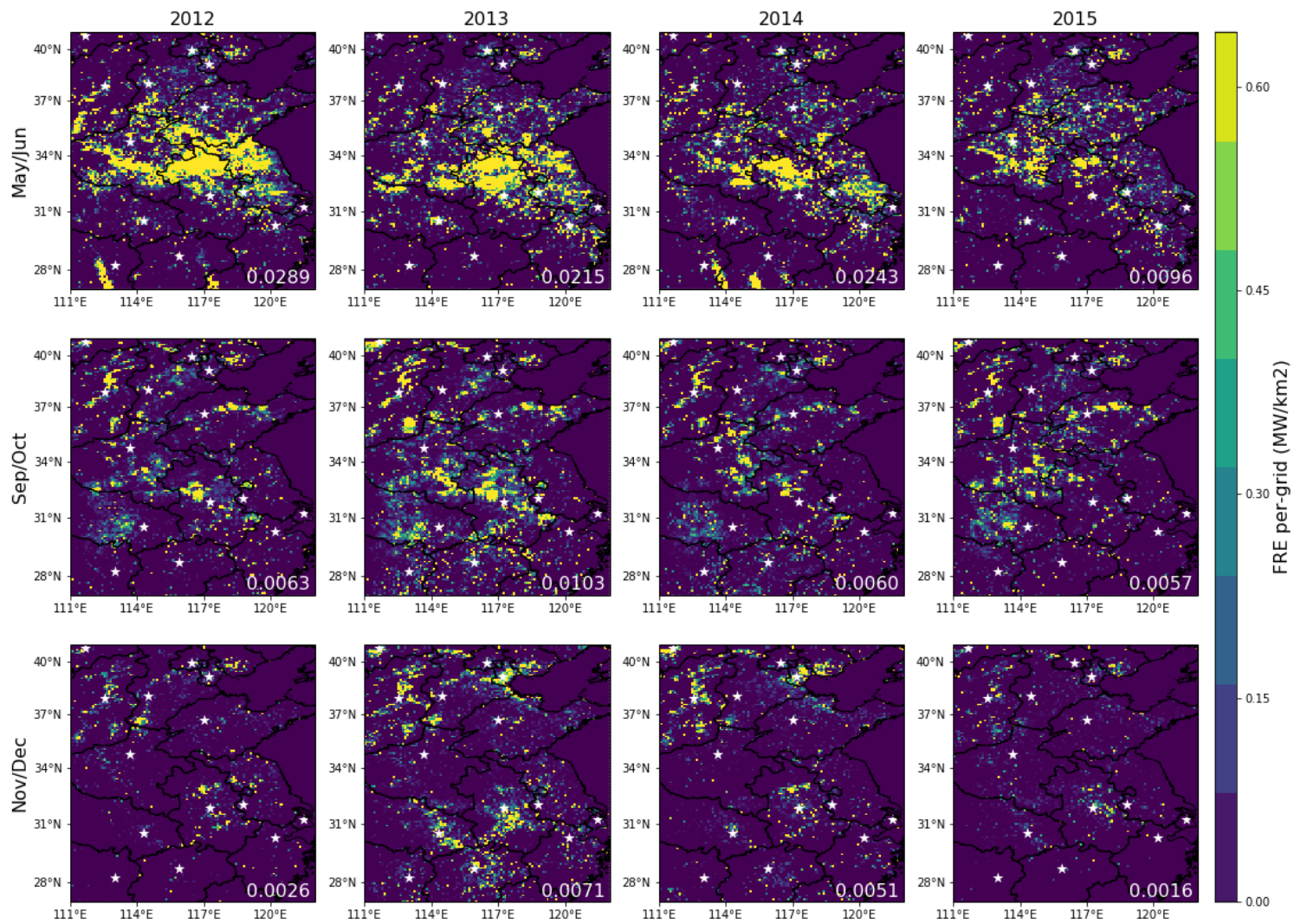
Figure 6: Spatial distribution of FRE areal density (MJ.m^{-2}, 0.1 deg grid cells) for agricultural fires in eastern China from 2012 to 2015 (top to bottom rows) split by fire season: summer (May-June, top row), autumn (Sep-Oct, middle row) and winter (Nov-Dec, bottom row). Mean regional FRE for each season is indicated

in white text, and the capital city location of each province is shown as a white star on each map. The basic layer of country/province borders within this map was created using Python Cartopy library.
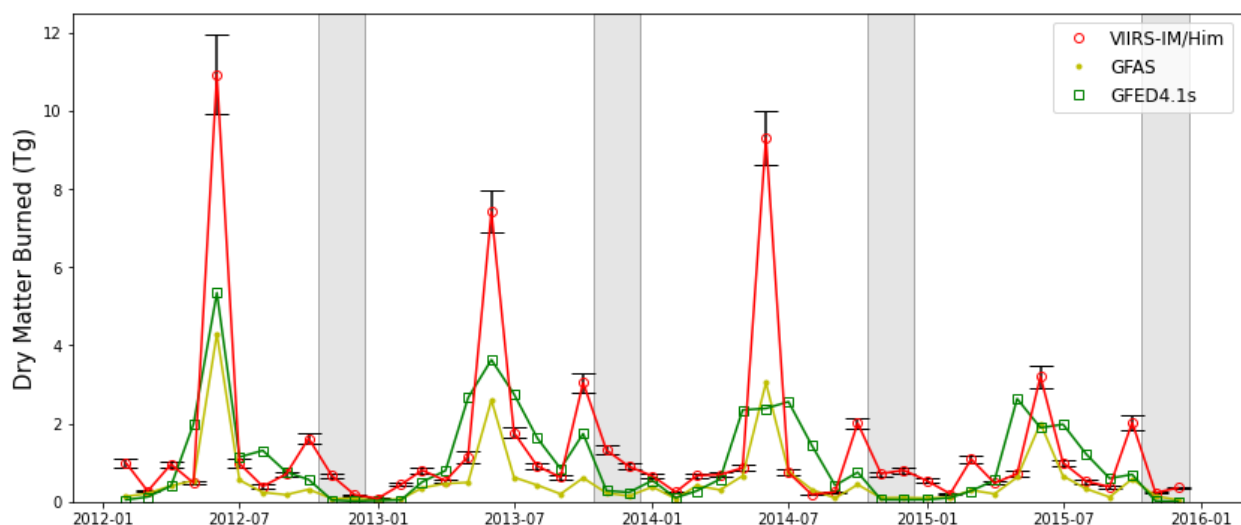
Figure 7: Monthly (2012-2015) time-series of total dry matter burned (DMB) retrieved using the VIIRS-IM/Him FRP product developed in this study (with standard deviation shown as black error bars), along with comparable GFAS and GFED4.1s DMB totals. Grey shaded areas highlighted the winter burning season from mid-November to December (Section 5.1).
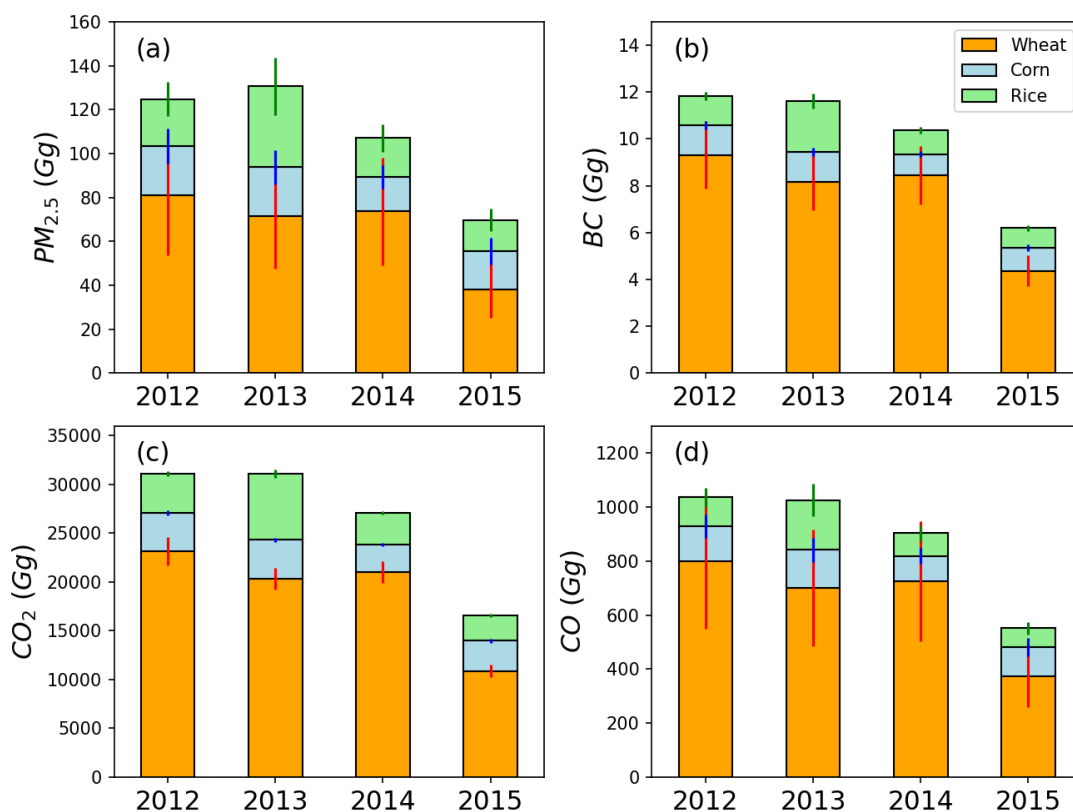
Figure 8: Annual total $PM_{2.5}$, BC, CO_2, and CO emissions for eastern China for the three main crop residues burning types (wheat, corn, rice) calculated for 2012-2015 using the VIIRS-IM/Him based emissions inventory developed herein. Coloured error bars indicate 1 standard deviation.
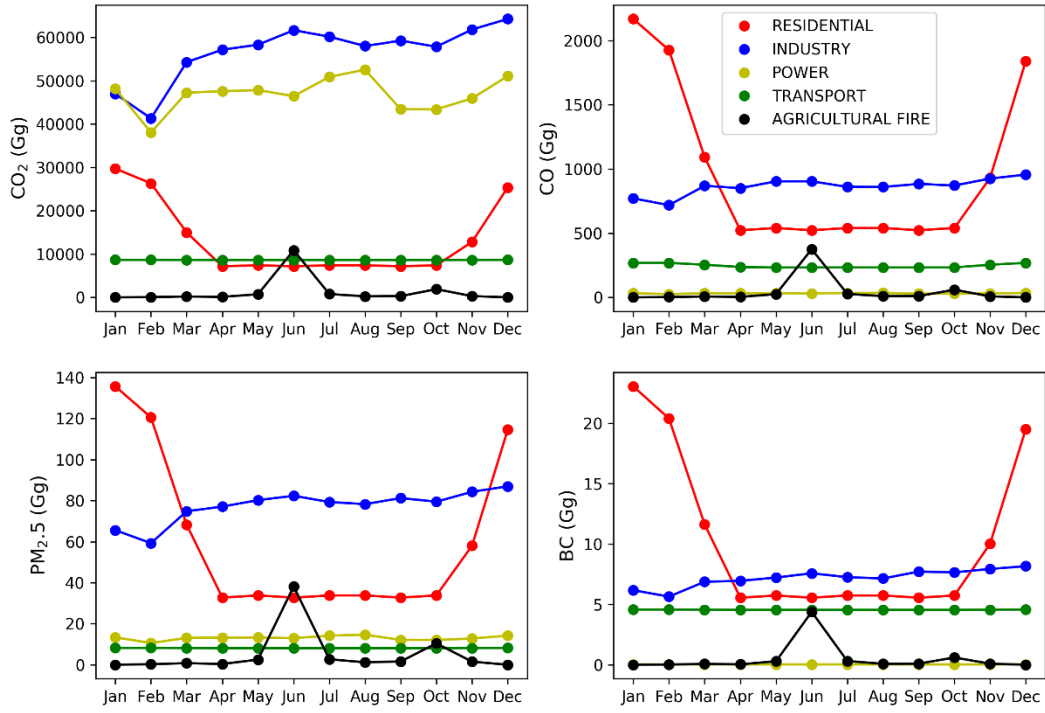
Figure 9: Comparison of monthly CO_2, CO, $PM_{2.5}$ and BC emissions from agricultural fires with those from other emission sources (residential, industry, power, transport, data source: Li et al., 2015) in the intensive burning area (32-36º N, 112-122º E) of eastern China in the year 2013.
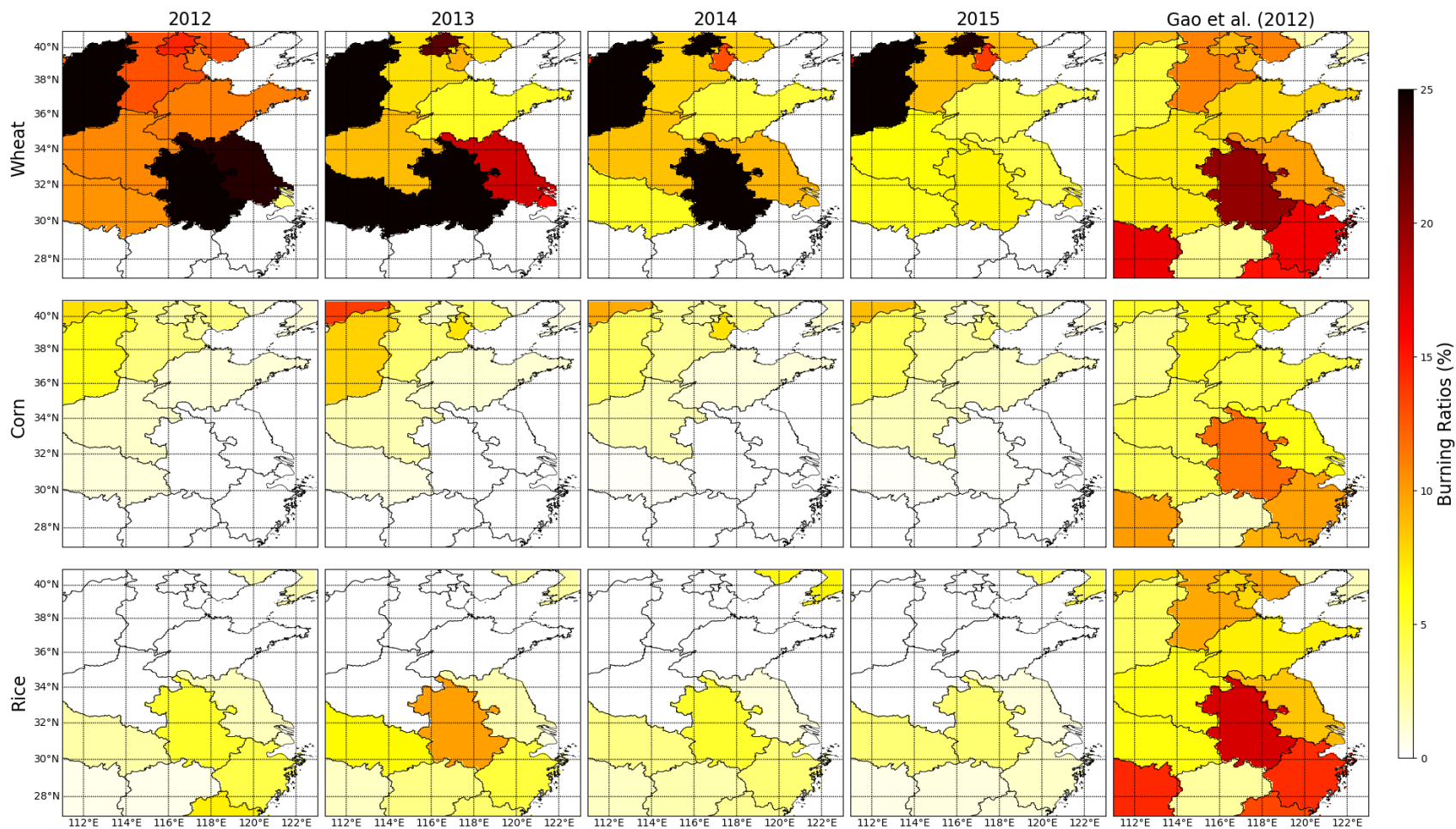
Figure 10: Temporal and spatial variability of province-specific percentages of crop residues burned in the fields (burning ratio metrics) of eastern China. Data are calculated using crop yield estimates from National Bureau of Statistics of China and the dry matter burned totals derived herein using our VIIRS-IM/Him DMB datasets from 2012-2015, and compared to the temporally invariant estimates provided by Gao et al., (2002, final column). The basic layer of country/province borders within this map was created using Python Basemap library.
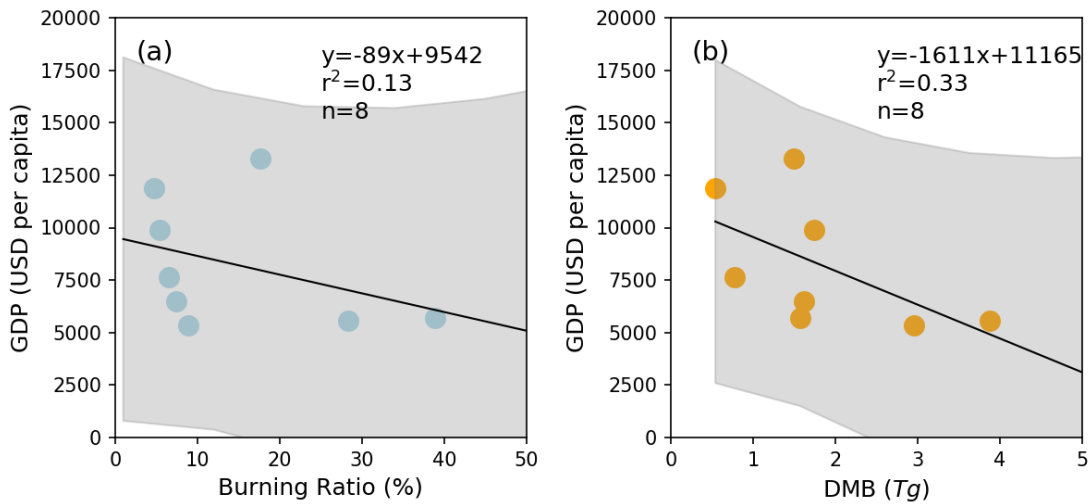
Figure 11: Direct comparisons of mean GDP per capita with (a) burning ratio for wheat from 2012, (b) province-specific yearly dry matter burned (DMB). The best fit linear relationships are shown, along with its equation, and the grey shaded area represents the 95% confidence limit on the relationship.
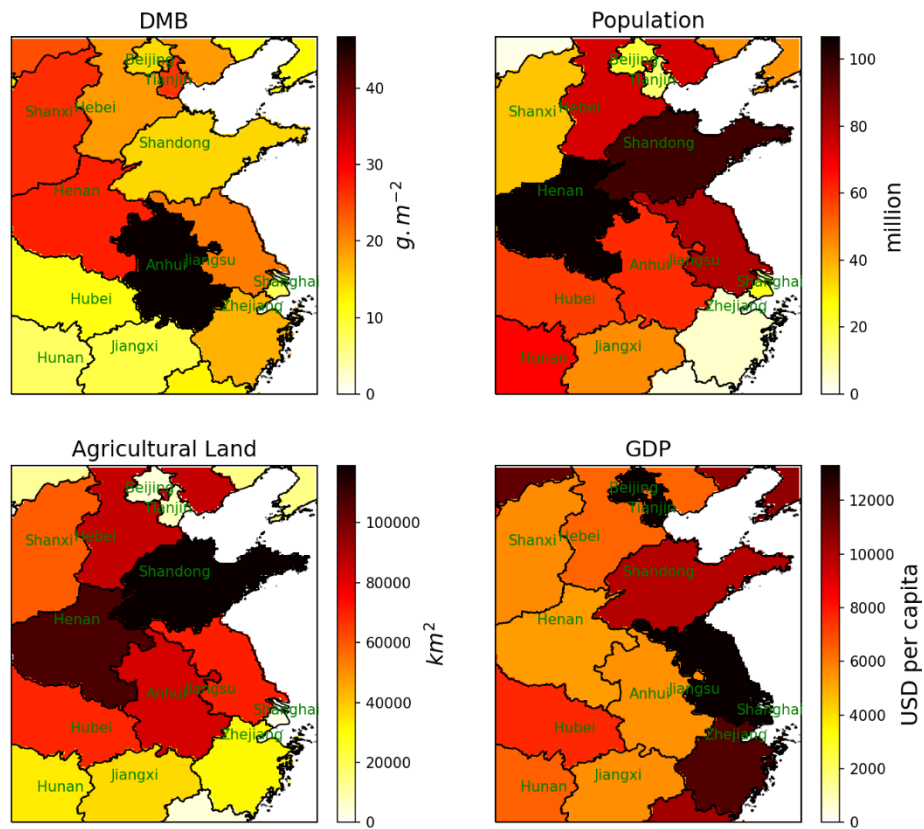
Figure 12: Spatial distribution of province-specific: (a) mean annual dry matter burned as calculated using the VIIRS-IM/Him approach developed herein, (b) population (Data source: Fu *et al.,* 2014a), (c) agricultural land area (Data source: GlobeLand30, http://www.globallandcover.com/) and (d) mean GDP per capita (Data source: Fu *et al.,* 2014b). The basic layer of country/province borders within this map was created using Python Basemap library.
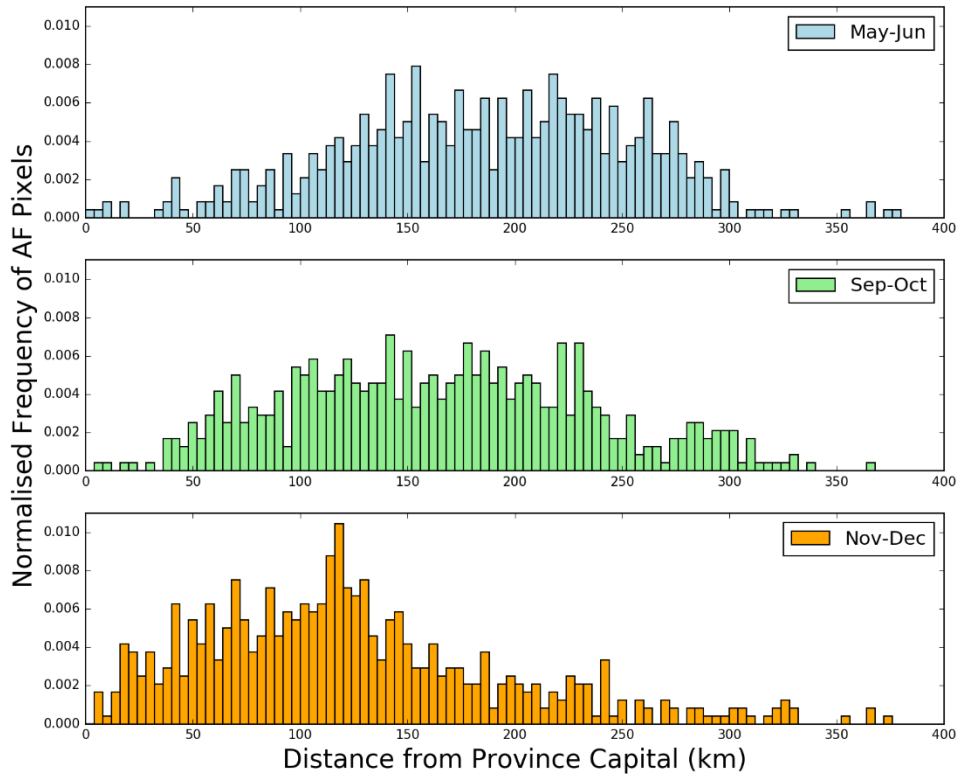
Figure 13: Normalised frequency distribution of distance from province capital of the top 10% of high FRE VIIRS-IM/Him product 0.1 degree grid cells during the three burning seasons: Summer - May to June (top, blue), Autumn – September to October (middle, green), and Winter - November to December (bottom, orange). A clear shift towards the origin can be observed in the Nov-Dec period compared with Sep-Oct.